

GEOCHEMISTRY, THERMOCHRONOMETRY, PETROGENESIS AND  
GEOMETRY OF IGNEOUS DIKES IN CENTRAL ARKANSAS:  
IMPLICATIONS FOR MISSISSIPPI EMBAYMENT EVOLUTION

by

SAMUEL REED WALKER

IBRAHIM CEMEN, COMMITTEE CHAIR  
MATTHEW WIELICKI, COMMITTEE CO-CHAIR  
BERRY H. TEW, JR.  
DANIEL STOCKLI

A THESIS

Submitted in partial fulfillment of the requirements  
for the degree of Master of Science  
in the Department of Geological Sciences  
in the Graduate School of  
The University of Alabama

2021

Copyright Samuel Reed Walker 2021  
ALL RIGHTS RESERVED

## **ABSTRACT**

The Mississippi Embayment (ME) is a south-plunging sedimentary basin which unconformably overlies the Cambrian Mississippi Valley Graben (MVG) and serves as a natural laboratory for extensional tectonics. The Arkansas Alkaline Province (AAP) lies along the ME's western border in central Arkansas and was emplaced in the mid-Cretaceous Period as a suite of intrusive bodies. The relationship between the ME and AAP, and a mechanism which generated both, remain unclear. To investigate this relationship and identify a petrogenetic mechanism, a multidisciplinary approach was used that involves geochemistry (major oxide and trace element, Nd isotopes), thermochronometry (U-Th/He), and geometry of 11 igneous dikes from the AAP. These data reveal that dikes are potassic-ultrapotassic and extremely enriched in incompatible elements relevant to OIBs and MORBs. Combined with data from other studies, the Nd isotopic ratio values demonstrate that lamprophyres were derived from asthenospheric magma unlike other intrusions. Despite depleted Nd isotope ratios, lamprophyres and every other sample reveal enrichment in incompatible elements and high Sr and Nb contents (indicative of carbonatite metasomatism). This decoupling between isotope ratios and trace element contents could represent low degrees of partial melting of a depleted asthenospheric source. The remaining samples show similar trace element slopes on normalized diagrams and were likely derived from a similar source with varying degrees of crustal contamination.

Despite geochemical similarities between samples and average OIB values, I propose a non-plume evolution for the AAP and ME related to edge-driven convection (EDC) associated with regional tectonics. At the time of the AAP's emplacement (106-89 Ma), EDC was at its highest velocity (80-100 Ma after the Atlantic Ocean and GOM started rifting). At this time, the proto-ME region was uplifted, and melt was guided along pre-existing weaknesses. This is corroborated by rose diagrams, which indicate strong similarities between dike trends and thrust plane trends. Results and interpretations from this study clarify a potential mechanism for alkaline magmatism during a pulse of volcanism in the Cretaceous. Moreover, this study places the ME and AAP within the framework of global tectonics in the Cretaceous Period and emphasizes the influence of regional processes on nearby lithospheric weaknesses.

## **DEDICATION**

This work is dedicated to my mother, Jennifer, and my father, David. Their undying support throughout the years has provided me with everything I've ever needed to be successful, and inspired me to pursue what I love doing, and nothing short of it.

## **LIST OF ABBREVIATIONS AND SYMBOLS**

Ab	albite
Ank	ankerite
Ap	apatite
Ar-Ar	argon-argon
Aug	augite
AAP	Arkansas Alkaline Province
AOT	Alabama Oklahoma Transform
Ba	barium
bdl	below detection limits
Bt	biotite
BmP	Bermuda mantle plume
BR	Bermuda rise
Cal	calcite
Ce	cerium
Di	diopside

DM	depleted mantle
EDC	edge-driven convection
EMI	enriched mantle I
EMII	enriched mantle II
Fsp	feldspar
GOM	Gulf of Mexico
Grt	garnet
Hbl	hornblende
Hf	hafnium
HFSe	high field strength elements
Jd	jadeite
K-Ar	Potassium-argon
Krs	kaersutite
Lct	leucite
LIL	large ion-lithophile
ME	Mississippi Embayment
MORB	mid ocean ridge basalt
MVG	Mississippi Valley Graben

Nb	niobium
Nd	neodymium
NGA	northern gulf anomaly
Nph	nepheline
OFB	Ouachita fold-thrust belt
OIB	ocean island basalt
Or	orthoclase
PAAP	Peri-Atlantic Alkaline Pulse
Pb	lead
PHEM	primitive helium mantle
Prv	perovskite
Rb-Sr	rubidium-strontium
RfR	Reelfoot Rift
Sa	sanidine
SCLM	sub-continental lithospheric mantle
Sdl	sodalite
SEM	scanning electron microscopy
Sm	samarium

Sr	strontium
Ta	tantalum
TAS	total alkali-silica
TER	trace element ratio
Th	thorium
TIMS	thermal ionization mass spectrometry
Ttn	titanite
Usp	ulvospinel
U	uranium
U-Pb	uranium-lead
(U-Th)/He	(uranium-thorium)/helium
XRF	x-ray fluorescence
Y	yttrium
Zeo	zeolite
Zr	zirconium
ZHe	zircon helium
°C	degrees Celsius
±	plus or minus

> greater than

< less than

% percent

## ACKNOWLEDGEMENTS

I firmly believe that conducting scientific research requires much more than one person. One could say that it “takes a village.” Thus, I would like to say thank you to all of the kind people who assisted me throughout this project. Firstly, I would like to thank my co-advisors, Drs. Ibrahim Çemen and Matthew Wielicki, who have guided me throughout the scientific process, helped develop my research skills, and continued to foster my passion for geological sciences. I also owe thanks to Drs. Danny Stockli and Nick Tew, for agreeing to serve on my committee and taking their own time to offer scientific advice and guidance. A special thanks is owed to Dr. Stockli’s lab group at UT-Austin, who spent a large amount of time processing my samples and producing data for this work. Dr. Harold Stowell and his students Hannah Dickson and Ian Anderson are also owed thanks due to their invaluable assistance with TIMS sample prep and analysis. A special thanks to Hannah for spending hours with me in the clean lab! Dr. Jade Star Lackey was a tremendous help with XRF sample prep and analysis, and we are indebted to his lab at Pomona College. Zach Yates was a huge help with sample collection and general support in April of 2019. Corbin Cannon and Ty Johnson at the Arkansas Geologic Survey were a huge help with sample collection, and this project would be nothing without them. I would also like to thank Jordan Faltys for providing hours of his own time for general advice and guidance in and outside the lab. Last but not least, I would like to thank Emily Schnarre for accommodating my incessant stress and anxiety and preserving my overall sanity throughout this process. Project funding was provided by The University of Alabama

School of Arts and Sciences, the Department of Geological Sciences, and the AAPG Hugh D. Miser Memorial Grant.

## CONTENTS

ABSTRACT.....	ii
DEDICATION.....	iv
LIST OF ABBREVIATIONS AND SYMBOLS.....	v
ACKNOWLEDGEMENTS.....	x
LIST OF TABLES.....	xv
LIST OF FIGURES.....	xvi
INTRODUCTION.....	1
GEOLOGIC OVERVIEW.....	7
The Mississippi Embayment.....	7
The Arkansas Alkaline Province.....	8
Emplacement Mechanisms for Alkaline Provinces.....	11
METHODS.....	15
Sample Collection and Mineral Separation.....	15
(U-Th)/He Analyses.....	16
Whole-rock Major and Trace Elements.....	16

Thick-section Analyses.....	18
Thermal Ion Mass Spectrometry.....	18
Paleo-stress Analyses.....	19
RESULTS.....	21
Major and Trace Elements.....	21
Nd Isotopic Geochemistry.....	32
(U-Th)/He Results.....	34
Petrography.....	34
Dike Orientations.....	39
Group 1 Dikes.....	39
Group 2 Dikes.....	42
Thrust Fault Orientations.....	43
Basement Fault Orientations.....	43
DISCUSSION.....	45
Role of Partial Melting, Fractional Crystallization, and Crustal Contamination.....	45
Mantle Sources and Metasomatism.....	46
Paleostress Regimes.....	49
AAP Petrogenesis.....	51

A Non-plume Mechanism for AAP Emplacement and ME Evolution.....	55
CONCLUSIONS.....	60
REFERENCES.....	64

## LIST OF TABLES

1. Whole-rock major and trace element data.....	22
2. Summarized (U-Th)/He age data.....	22
3. Summarized Nd TIMS data.....	22

## LIST OF FIGURES

1. Map of regional tectonic features.....	4
2A. Mississippi Embayment cross section.....	5
2B. Schematic diagram of a proposed mantle plume origin for the AAP and ME.....	5
2C. Schematic diagram of a proposed non-plume origin for the AAP and ME.....	5
3A. Geologic map and digital elevation model of AAP sample locations.....	6
3B. Geologic map and digital elevation model of Magnet Cove sample locations.....	6
4. Summarized emplacement ages for the AAP with major tectonic events.....	10
5A. Field image of sample AB1910.....	17
5B. Field image of sample AB1909.....	17
6. Harker plots of MgO vs. various whole-rock major oxides and trace elements.....	23
7. TAS diagram (SiO <sub>2</sub> vs. Na <sub>2</sub> O+ K <sub>2</sub> O) for samples with lithologic boundaries.....	24
8. Na <sub>2</sub> O vs. K <sub>2</sub> O plot with series fields.....	25
9. AFM diagram for the samples.....	25
10. Normalized trace element spider diagrams.....	28

11A. Ce vs. Ce/Pb diagram.....	30
11B. Nb vs. Nb/U diagram.....	30
12A. Ba/Rb vs. Rb/Sr diagram with amphibole and phlogopite fields.....	31
12B. Zr/Y vs. Nb/Y with mantle reservoir and plume vs. non-plume fields.....	31
13. Plot of $^{143}\text{Nd}/^{144}\text{Nd}$ isotopic ratio values and mantle reservoirs.....	33
14. Backscattered electron images of samples with mineral annotations.....	35
15. Digital elevation map and plot of rose diagrams for igneous dikes and thrust planes.....	41
16. Digital elevation map and plot of rose diagrams for basement faults.....	42
17A. La/Sm vs. Nb with metasomatizing agent vectors.....	49
17B. La/Sm vs. Sr with metasomatizing agent vectors.....	49
18. Schematic representation of EDC.....	60
19. Model of ME/AAP evolution through EDC and Atlantic rifting.....	62
20. Model of ME/AAP evolution through EDC and GOM opening.....	63

## INTRODUCTION

The relationship between magmatism and tectonics in intraplate settings has proven enigmatic. It is well-documented that pre-existing tectonic features such as rift zones can serve as pathways that guide melt into the overlying crust (Loper, 1998; Matton and Jebrak, 2009). However, there is still debate over the exact mechanism that allows magma to intrude so far away from plate boundaries, whether it be sudden changes in a regional stress field, or a mantle plume that intrudes into the continental crust. The latter explanation – the plume hypothesis – involves an upwelling mass of material in the mantle (Condie, 2001). As a tectonic plate passes over a plume, magma is injected into the crust, leaving a long trail of igneous provinces terminating in a currently active “hotspot” region (Loper, 1996).

Igneous provinces along a hotspot track usually exhibit similar lithologies and geochemical signatures. Proposed hot spot tracks commonly feature igneous rocks of the alkaline variety, which can be found in anorogenic and within-plate settings and are related to rifting/extensional tectonics. Suites of alkaline igneous rocks are found in North and South America, and Africa, with nearly all of them concentrated along pre-existing structures related to opening of the Iapetus Ocean during the Late Proterozoic and Early Cambrian (Matton and Jebrak, 2009). These intrusive complexes mark a period of increased alkaline activity in the mid-Cretaceous that has been attributed to either deep mantle plume activity in the form of a “superplume” event (Larson, 1991a), or periodic reactivation of pre-existing lithospheric weaknesses due to edge-driven convection (EDC) processes (Matton and Jebrak, 2009).

A particular alkaline province in Central Arkansas known as the Arkansas Alkaline Province (AAP), lies along proposed age-progressive tracks for the Bermuda hotspot (Fig. 1) (Duncan, 1984; Muller et al., 1993). The proposed track is comprised of igneous intrusions in Kansas, central Arkansas, and Mississippi, and is believed to terminate at the Bermuda swell in the central Atlantic Ocean. There are no known igneous rocks in Alabama or Georgia that contribute to, or “complete”, an age-progressive track of volcanism.

The AAP is also located at the junction between two structures – the Early Cambrian Reelfoot Rift (RfR) and the orthogonal Alabama-Oklahoma Transform (AOT), which were both formed during the opening of the Iapetus Ocean (Thomas, 2011). Unconformably overlying the RfR are Cretaceous and Cenozoic sedimentary rocks and alluvium of the Mississippi Embayment (ME), a south-plunging topographic depression that serves as a northward continuation of the Gulf of Mexico (GOM) coastal plain. Members of the AAP lie along the ME’s western border in Central Arkansas. Thus, the AAP serves as a natural laboratory for studying emplacement mechanisms of alkaline provinces and examining the competing hypotheses that explain their evolution.

The purpose of this study is to test two competing hypotheses regarding the ME’s structural evolution. Hypotheses are tested by studying igneous intrusions of the AAP, with an emphasis on their petrogenesis and tectonic significance, especially their implications for the ME’s formation. Geochemical data for eleven samples – collected in Central Arkansas in April 2019 - are presented in the form of whole-rock major oxides and trace elements. Whole-rock neodymium (Nd) isotopes from four representative samples are also presented and discussed to identify the origin of sampled rocks. Scanning electron microscopy (SEM) images as well as Energy Dispersive Spectroscopy (EDS) are used to investigate sample mineralogy and

corroborate XRF results. In unison with the geochemical data, orientations of over 700 igneous dikes throughout the AAP are presented as rose diagrams. These diagrams were used to investigate stress regimes during AAP emplacement and demonstrate the tectonic significance of igneous intrusion orientations. Finally, thermochronology (Zircon U-Th/He) data from 5 samples is also presented. Results from this study enhance the current understanding of the AAP's genesis and emplacement, and its associated effects on the structural evolution of the Mississippi Embayment. Techniques and interpretations developed in this study can be applied to other rift zones in efforts to understand the interplay between extensional tectonics and alkaline magmatism related to basin evolution. Moreover, this study clarifies the mechanism by which numerous alkaline provinces across the world were emplaced in the crust during a "pulse" of increased alkaline magmatism in the Cretaceous Period.

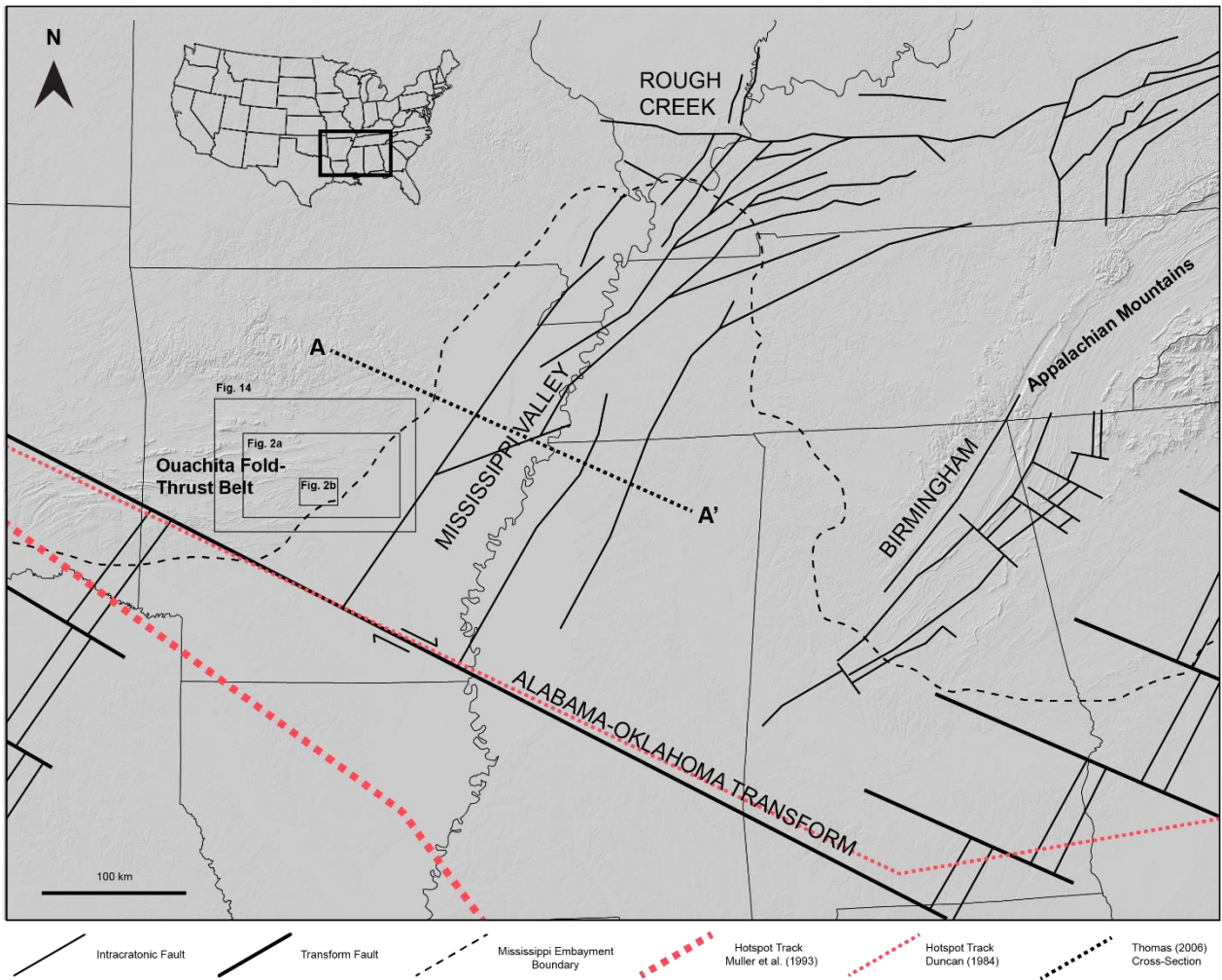
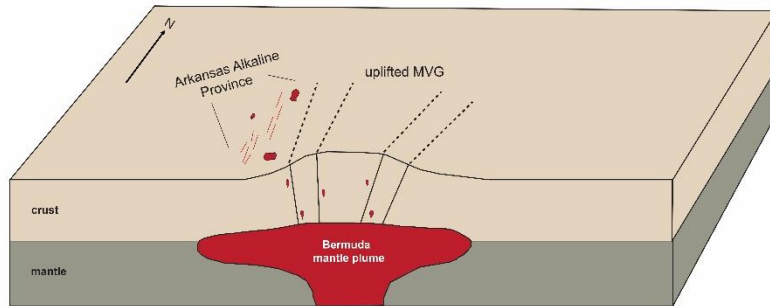


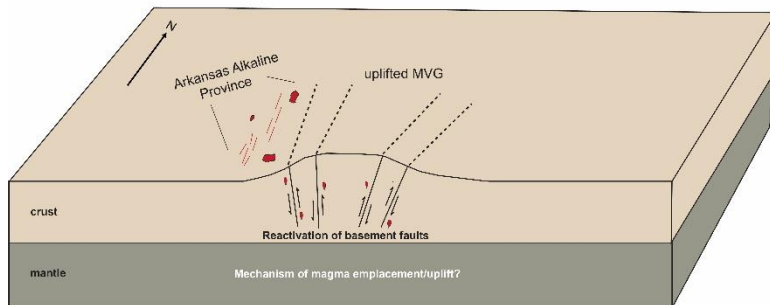
**Figure 1.** Digital elevation map of the south-central United States, with regional tectonic features after Thomas (2006) and hot spot tracks after Muller et al. (1993) and Duncan (1984). Locations of the Ouachita Fold-Thrust Belt and Appalachian Mountains are indicated as well as the location of extensional grabens. Locations of Figures 2 and 14, and a cross section transect from Thomas (2011) are indicated. The digital elevation map is taken from the USGS National Map. The map projection is NAD\_1983\_UTM\_Zone\_15N.

1

A) Hypothesis #1: Mantle plume hypothesis for ME and AAP evolution



B) Hypothesis #2: Non-plume/rift-reactivation hypothesis for ME and AAP evolution



C) Current configuration of the Mississippi Embayment

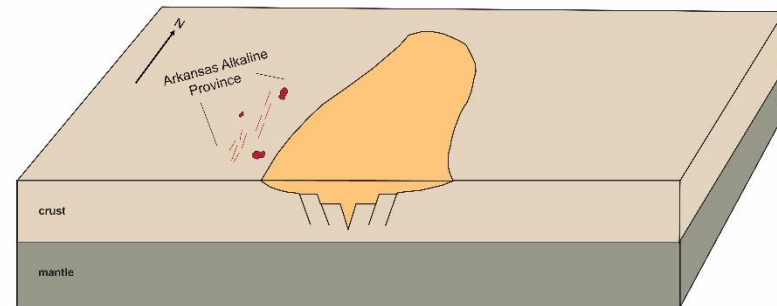


**Figure 2.** Schematic diagrams indicating the current structure of the Mississippi Embayment, and alternate hypotheses concerning its evolution: (a) mantle plume hypotheses after Cox and Van Arsdale (1996; 2002) which suggests that a mantle plume uplifted the proto-ME and is responsible for its evolution, (b) non-plume hypotheses for ME evolution which relies on the reactivation of MVG faults and does not require a mantle plume for ME evolution (after Ervin and McGinnis, 1975; Eby and Vasconcelos, 2009), (c) current configuration of the Embayment. The transect for the cross sections in the foreground of these schematics is indicated by the A-A' line in Figure 1.

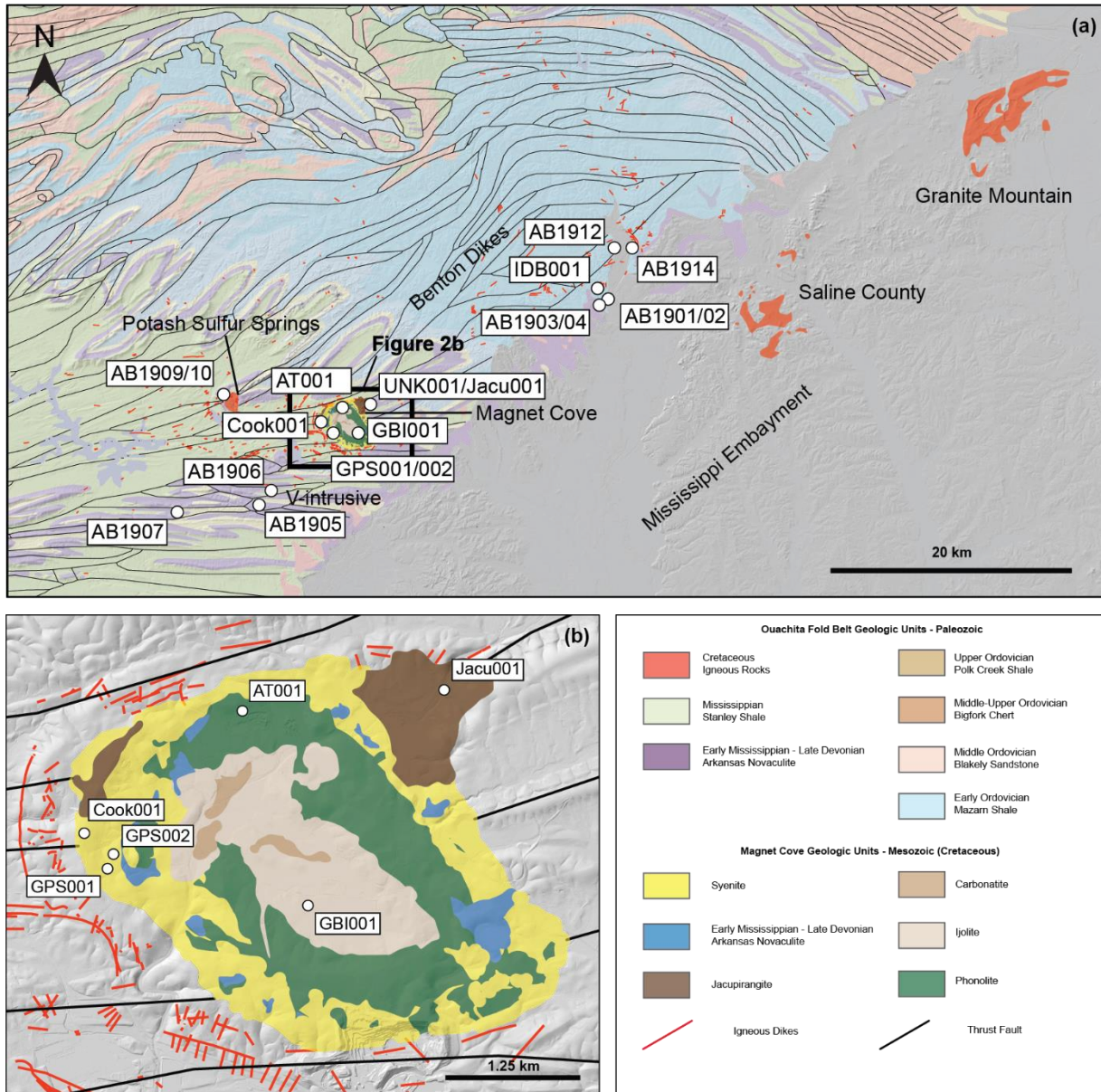


**Figure 3.** Digital elevation maps and geologic overlays for (a) the OFB with sample locations and each specified member of the AAP, and (b) a map of the Magnet Cove intrusive ring-dike complex with sample locations. Geologic overlays are from the Arkansas Geological Survey database and Erickson and Blade (1963). The digital elevation map is after the USGS National Map. Map projection is NAD\_1983\_UTM\_Zone\_15N.

## **GEOLOGIC OVERVIEW**

### **The Mississippi Embayment**

The Mississippi Embayment (ME) is a southwest-plunging depression extending from southern Illinois to Louisiana (Fig. 1). At its eastern border in Arkansas, the ME is bordered by the folded and faulted lower to middle Paleozoic rocks of the Ouachita fold-thrust belt (OFB) and Pennsylvanian rocks of the Arkoma Basin. To the east, the ME is bordered by the southern Appalachian Mountains in Alabama (Thomas, 1985).

The southern half of the Embayment serves as the northward extension of the Gulf of Mexico coastal plain, containing 1.5 km of Mesozoic and Cenozoic sedimentary rocks. The northern ME overlies Paleozoic cratonic shelf facies that range between Cambrian and Pennsylvanian in age. Units of the southern ME overlie rocks of the Ouachita orogeny which were thrust over the Paleozoic craton. The basin fill is comprised of marine and deltaic sediments that are Late Cretaceous and Late Eocene in age. These sediments are thickest in the southern portion of the basin, where 2 km of Upper Cretaceous to Upper Eocene sediments are overlain by Pliocene and Quaternary fluvial deposits (Stearns, 1957; Murray, 1961; Cushing et al. 1964; Autin et al., 1991; Hosman and Weiss, 1991; Cox et al., 2002). These sediments are < 1 km thick in the northern ME, where they overlie the RfR. Pre-Late Cretaceous strata of the ME's basin fill extend to central Arkansas and into western Mississippi where they terminate into Ouachita Fold Belt (OFB) rocks and Lower Cretaceous units of the Hosston Group in Mississippi (Murray, 1961; Schwalb, 1982; Howe, 1984). Mooney et al. (1984) used seismic refraction to suggest that

the crust of the ME is comprised of 6 primary layers, which include: Mesozoic and Tertiary sediments, underlying Paleozoic clastic and carbonate rocks, Early Paleozoic sedimentary rocks, crystalline upper crustal rocks, lower crust, and a modified lower crust.

Structurally, the ME is a broad synclinal feature that plunges gently to the southwest where it continues throughout the coastal plain. Its base forms an unconformable contact with the underlying RfR sedimentary rock units (usually referred to as the Mississippi Valley Graben: MVG). The RfR is a NE-SW trending intracratonic rift that lies nearly perpendicular to the NW-SE trending Alabama-Oklahoma transform (Fig. 1), which serves as the Late Precambrian-Cambrian Iapetan rifted margin in that area (Thomas, 2011). Normal faults of the RfR cut Precambrian metamorphic basement rocks, Lower and Middle Cambrian units, Upper Cambrian – Lower Ordovician units, Middle Ordovician – Middle Mississippian Units, and Pennsylvanian – Upper Mississippian sedimentary rock units of the OFB in central Arkansas (Fig. 2a). Exact depths of each normal fault are uncertain as there is no bio-stratigraphic documentation for deeper unit (Thomas, 2011). End of RfR fault movement is indicated by faulted strata of the Conasauga formation that are blanketed by the Upper Cambrian-Lower Ordovician Knox Group (Thomas, 1991). The faulted units form a broad anticlinal structure that trends NE-SW and plunges southwest, similar to the ME's synclinal structure (Murray, 1961). The upper portion of the anticline's crest is non-existent and forms an angular unconformity with overlying ME units (Fig. 2a).

### **The Arkansas Alkaline Province**

The AAP is a northeast-trending suite of intrusive igneous bodies that lies adjacent to the Mississippi Embayment's western border. Igneous members of the AAP intrude lower to middle Paleozoic rocks of the OFB. From the southwest in Murfreesboro, AR to the northeast near Little

Rock, the intrusive suites are referred to as Prairie Creek, Magnet Cove, V-Intrusive, Potash Sulfur Springs, Benton Dikes, Saline County, and Granite Mountain, respectively (Fig. 3a). Thin carbonatite dikes are present 80km north of the Magnet Cove Complex in Morrilton and Perryville, AR (McCormick and Heathcote, 1979). AAP members occur as large plutonic bodies (Magnet Cove, Potash Sulfur Springs, Saline County, Granite Mountain) or smaller dikes (Benton, V-intrusive) that crosscut Paleozoic strata. Lithologies vary between carbonatite, ijolite, jacupirangite, lamproite, lamprophyre, kimberlite, and nepheline syenite (Morris, 1987; Eby and Vasconcelos, 2009). A general geographic progression in lithologies is evident, with more ultramafic intrusions (lamprophyres, lamproites, ijolites, jacupirangites, kimberlites, carbonatites) to the southwest and more evolved, felsic rocks (nepheline syenites) found near the AAP's northeastern corner.

Multiple studies (Fig. 4) have used radiometric age-dating techniques (K-Ar, Ar-Ar, U-Pb, Rb-Sr, Fission track) to determine the age of emplacement for the assorted AAP intrusions. Ages from these studies fall primarily within the middle Cretaceous Period (106 – 88 Ma) (Eby and Vasconcelos, 2009). A rough SW-NE progression in age is evident for the AAP, with older intrusions (> 100 Ma) in the southwest AAP, and younger intrusive bodies (< 90 Ma) to the northeast. Eby and Vasconcelos (2009) divided these ages into three primary time frames: > 100 Ma, 100-90 Ma, and < 90 Ma. A correlation between lithology and age is apparent, with emplacement ages of ~106 Ma for lamproites, 101-94 Ma for carbonatites and other ultramafic rocks, and ~88 Ma for nepheline syenite intrusions (Eby and Vasconcelos, 2009).

The genesis of AAP igneous bodies and their emplacement mechanisms remain unclear. Due to diverse lithologies for AAP members, it is necessary to investigate the petrogenesis of each

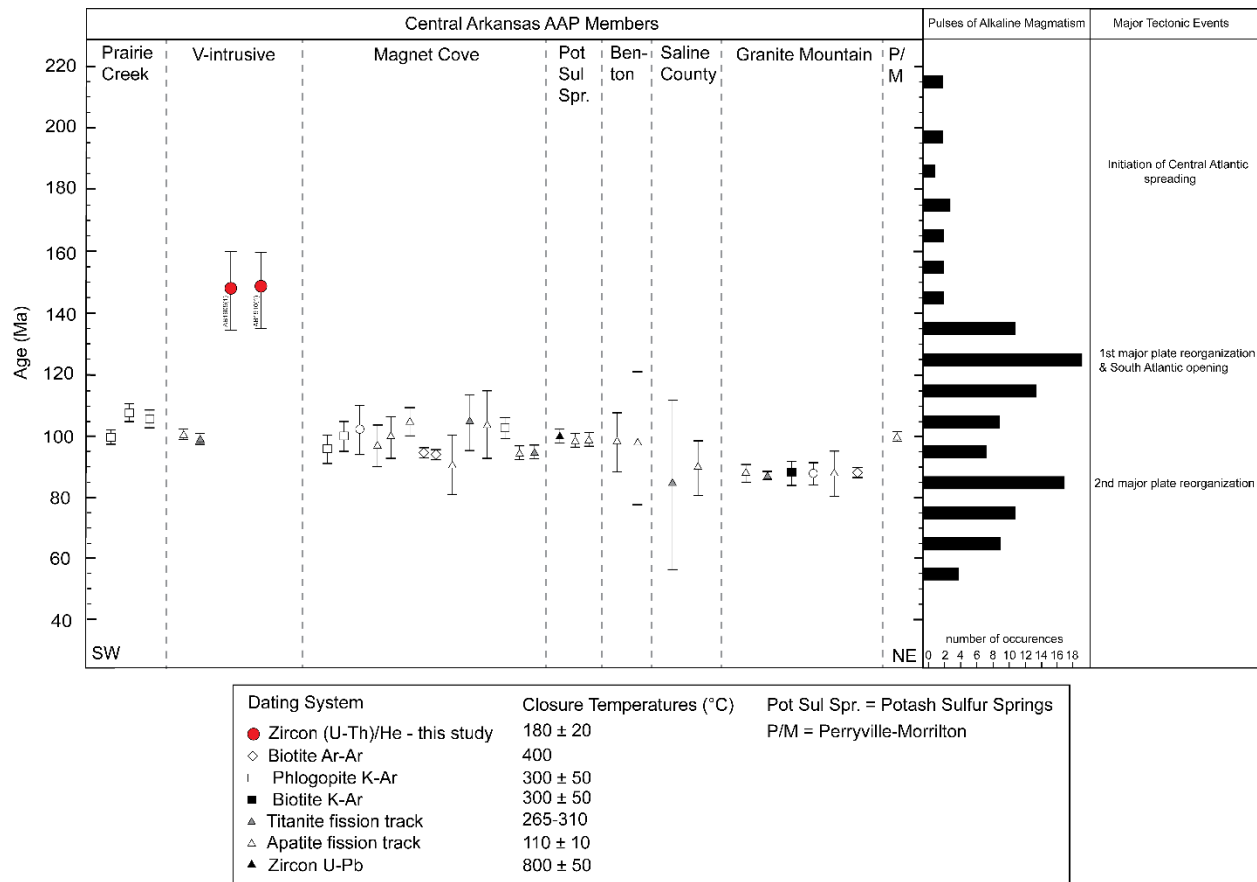


**Figure 4.** Summary plot of age data presented in previous studies (Biotite Ar-Ar: Baksi, 1997; Phlogopite K-Ar: Zartman, 1977; Gogineni et al. 1978; Biotite K-Ar: Zartman et al. 1967; Titanite fission track: Scharon and Hsu 1969, Eby and Vasconcelos, 2009; Apatite fission track: Arne, 1992, Scharon and Hsu, 1969; Eby and Vasconcelos, 2009; Zircon U-Pb: Zartman and Howard, 1987) and (U-Th)/He data for this study. A histogram demonstrating timing and frequency of alkaline magmatism and associated Atlantic tectonic events are presented (from Eby and Vasconcelos, 2009).

complex separately to comprehensively understand the greater magmatic system behind AAP evolution. Previous studies (Morris et al., 1987; Tilton et al., 1987; Duke et al., 2008) have utilized isotopic data for this purpose. These studies indicate that multiple magma sources and processes were likely involved in AAP evolution. Sr, Nd, and Pb isotopic values of olivine lamproites from Prairie Creek ( $\epsilon_{Nd} = -10$  to  $-13$ ,  $^{206}Pb/^{204}Pb = 16.61-16.81$ ,  $^{87}Sr/^{86}Sr = 0.70627-0.70829$ ) and Dare Mine Knob ( $\epsilon_{Nd} = -19$ ) reflect a sub-continental lithospheric mantle (SCLM) origin and involvement of a significant crustal component (Duke et al., 2008). Sr-Nd-Pb isotopic

values from Magnet Cove carbonatites ( $^{143}\text{Nd}/^{144}\text{Nd} = 0.51271$ ,  $^{87}\text{Sr}/^{86}\text{Sr} = 0.70363$ ,  $^{206}\text{Pb}/^{204}\text{Pb} = 15.549$ ) indicate little crustal involvement and an asthenospheric source that's depleted in large ion-lithophile (LIL) elements (Tilton et al., 1987).

### **Emplacement Mechanisms for Alkaline Provinces**

Alkaline igneous provinces are ubiquitous and are found in anorogenic and within-plate settings, usually related to rifting/extensional tectonics. Similar to the AAP, a large portion of alkaline provinces were emplaced in the mid-Cretaceous Period, which Matton and Jebrak (2009) refer to as the Peri-Atlantic Alkaline Pulse (PAAP). Thus, the mid-Cretaceous Period represents an increased flare in alkaline igneous activity which has been attributed either to the influence of mantle plumes or structural control related to reactivation of pre-existing lithospheric weaknesses.

Matton and Jebrak (2009) tested the validity of plume and structural models by examining PAAP provinces in eastern North America, eastern South America, and western Africa. Nearly all of the PAAP alkaline provinces are situated near pre-existing zones of weakness such as rift systems, including aulacogens (senso-lotto), grabens, large normal faults, etc., which are pre-Cretaceous in age. This is also the case for the AAP, which is located at the junction between the NE-SW oriented RfR and the orthogonal AOT; two large-scale structures related to the opening of the Iapetus ocean. Reactivation of these pre-existing features has been documented for some PAAP members including Pan-African related structures in Africa, Iapetus-related structures in eastern North America, Precambrian weaknesses in South America, and Variscan-related lineaments in western Iberia (Matton and Jebrak, 2009). Comparing the emplacement ages of the AAP and the PAAP with tectonic evolution of the Atlantic Ocean (see Figure 4), Matton and Jebrak (2009) suggested that the PAAP is best described by the

reactivation of pre-existing features due to edge-driven convection (EDC). EDC was initially described by King and Anderson (1998) as an instability that take place between thick lithosphere and thinner lithosphere. The temperature gradient along the thick lithosphere's boundary drives convection cells, which are confined to the upper mantle (King and Anderson, 1998). In this hypothesis, two major tectonic events at ~85 Ma and ~125 Ma correlate strongly with spikes in PAAP occurrences. Thermodynamic requirements for melting and emplacement of PAAP provinces were provided by continental insulation – allowing accumulation of mantle heat beneath the lithosphere - in the Early Cretaceous Period during breakup between South America and South Africa, followed by EDC between North America and West Africa (Matton and Jebrak, 2009).

An alternate explanation for the existence of alkaline provinces involves the influence of mantle plumes. Larson (1991a) attributed the increase in mid-Cretaceous alkaline activity to a “superplume” event. A superplume is an abnormally large mantle plume head (500 – 3000 km in diameter) (Condie, 2001). Thus, a superplume event is a short-lived (less than 100 Ma) event characterized by increased convection and hotspot volcanism. During such an event, many superplumes and smaller plumes impact the base of the lithosphere and intrude into zones of weakness (Condie 2001). Larson (1991a) used this model to explain a 50-75% increase in the rates of oceanic crust formation between 120 and 80 Ma. Other authors (e.g. Morgan, 1971; Burke and Dewey, 1973; Wilson, 1997; Leitch et al. 1998; Duncan, 1984; Muller et al. 1993) use the plume hypothesis to explain the opening of the Atlantic Ocean and emplacement of associated igneous bodies.

Mantle plumes are commonly linked to “hotspots,” or surface expressions of underlying mantle plumes. As continents drift over plumes, upwelling material is periodically emplaced in

the crust. Igneous material emplaced from mantle plumes should form an age-progressive track of volcanism which ends at an active hotspot, forming a “hotspot track” (Loper, 1996). Although there is no volcanic expression at its current location in the Atlantic Ocean (due to suggested volcanic inactivity over the last 20-30 Ma), the Bermuda Rise (BR) has been explained by multiple mantle plume models (Davies, 1988; Sleep, 1990). Some researchers (Morgan, 1983; Duncan, 1984; Muller et al., 1993) link the BR with igneous provinces in North America, suggesting that these provinces form an age-progressive hotspot track terminating at the BR.

A more direct influence of a mantle plume on the AAP and ME was first proposed by Cox and Van Arsdale (1997; 2002). They suggested that the AAP lies along a southeastward age progressive track of volcanism (Fig. 1) ending at the BR. This track begins with ultramafic intrusions in eastern Kansas (115 Ma – Brookins and Naeser, 1971; Crough et al. 1980; Cullers et al. 1996) and continues within the ME with the AAP (106-88 Ma – Eby and Vasconcelos, 2009 and references therein) and the Jackson Dome (65 Ma – Dockery et al., 1997) intrusive in central Mississippi. Ultramafic rocks in Kansas are situated within the sedimentary cover above the Proterozoic Central North American Rift System (CNARS) (Burchett et al., 1985), similar to AAP intrusions which lie just west of the Early Cambrian RfR. There are no known igneous rocks in Alabama or Georgia which contribute to an age-progressive track of volcanism.

Although some plutonic igneous rocks have been encountered in wells in south Alabama, K-Ar ages of these rocks ( $267 \pm 10$  Ma for basalt and  $334 \pm 4.8$  Ma for granite – Neathery and Thomas; 1975) are significantly older than the Jackson Dome province (65 Ma – Dockery et al., 1997) and therefore don't complete an age-progressive track. Based on this track, the model of Cox and Van Arsdale (1997; 2002) indicates westward passage of the North American continent over the Bermuda hot spot in the mid-Cretaceous Period. At this time, AAP intrusions were emplaced in

the crust and the region of the proto-ME was uplifted on the order of 1-3 km. As North America moved away from the hotspot in the Late Cretaceous Period, the uplifted crust was eroded, and subsidence of the ME began.

## METHODS

### Sample Collection and Mineral Separation

The dataset is multidisciplinary and comprised of geochemical data (whole-rock major oxides, trace elements, and Nd isotopes), petrographic data (thick sections), thermochronology and structural data (igneous dike geometries). Eleven samples were analyzed for their whole-rock major and trace element compositions and imaged with scanning electron microscopy. Four of the twelve samples were analyzed for their Nd isotopic compositions. Due to the wide range in lithology of the AAP, samples were selected to adequately cover the mineralogical range and magmatic processes in a representative fashion. Five samples were also dated via zircon (U-Th)/He.

Twenty-one samples were collected from the Ouachita fold and thrust belt in central Arkansas. Due to the high silica content of 8 samples – suggesting a non-igneous origin - and two float samples (AB1908, AB1911), only data for the remaining 11 samples is discussed in this study. Sample locations form a roughly NE-SW transect from Little Rock just southwest of Magnet Cove, AR along the ME's western border (Fig. 3a). Localities suitable for sampling were determined using field guidebooks and shapefiles provided by the Arkansas Geological Survey (AGS) and verbal communication with the AGS. Sampling locations were determined primarily by navigability of the terrain and available rock exposure (Fig. 2). Due to a wide range in lithologies, an effort was made to represent the numerous volcanic suites that comprise the AAP. Samples GPS001, GPS002, AT001, Cook001, UNK001, JACU001, and GBI001 were

collected from the Magnet Cove ring-dike complex in the southwest AAP (Fig. 2b). AB1909 and AB1910 were sampled from a roadcut from the V-intrusive dike swarm (Fig. 3a). The Benton Dike Swarm is represented in this study by samples IDB001, AB1912, and AB1914 (Fig. 3a).

### **(U-Th)/He Analyses**

Zircons were separated from bulk rock samples by standard mechanical, heavy liquid, and magnetic separation techniques. For thermochronology analyses, euhedral, inclusion-free zircon grains were picked and placed in petri dishes on double-sided tape and sent to the Geo- and Thermochronometry Laboratory at the University of Texas at Austin. Individual grains were first placed into 1-mm foil tubes, crimped on both ends, and heated for 10 minutes at 1300° C. An ultra-high vacuum noble gas extraction and purification line was used to measure the <sup>4</sup>He gas from each grain. After degassing, aliquots are dissolved to determine U, Th, and Sm. Ages were calculated applying standard  $\alpha$ -ejection corrections with morphometric analyses (Reiners, 2005).

### **Whole-rock Major and Trace Elements**

Bulk-rock samples were prepared adhering to the double fusion technique with a 2:1 di-lithium tetraborate mixture as outlined in Johnson et al. (1999). Fresh, homogeneous portions of each sample were cut out using a diamond-tip saw before being pulverized into powder using a low carbon steel ring and puck mill in a SPEX shatterbox. The powdered samples were then weighed and mixed with Spectromelt di-lithium tetraborate flux before fusion in graphite crucibles at 1000° C for 10 minutes. The glass beads were powdered again using the ring and

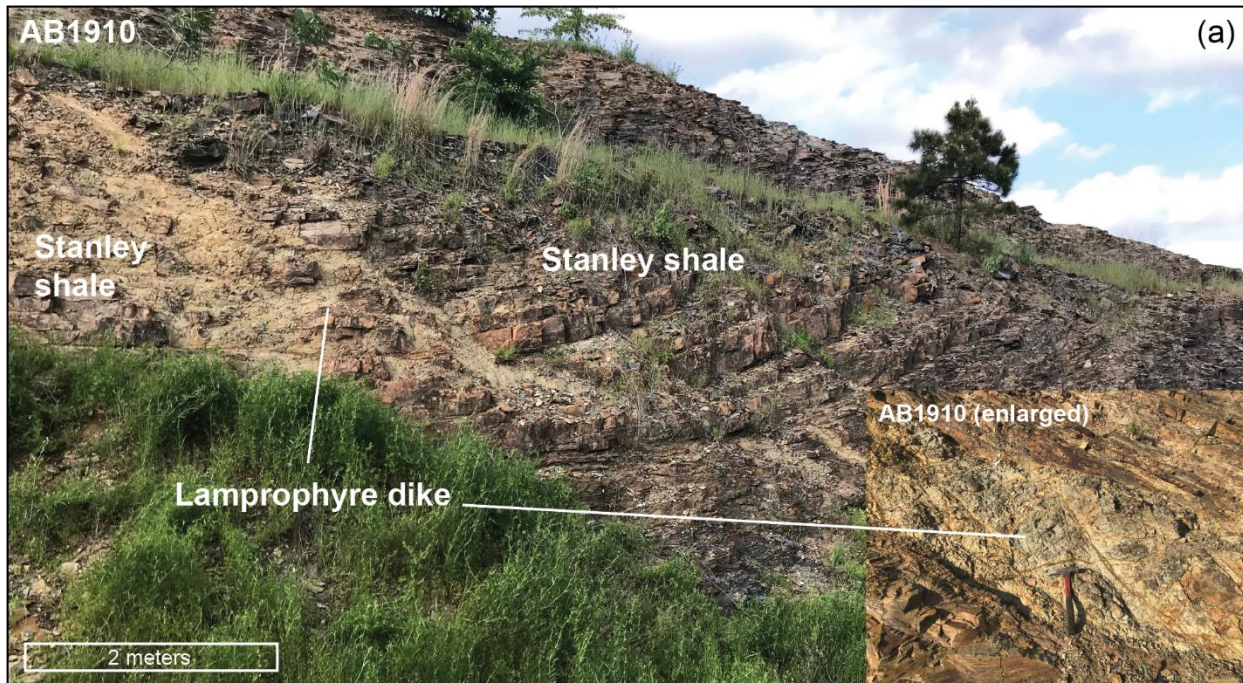


**Figure 5.** Field images for (a) sample AB1910 with an indicated lamprophyre dike intruding the Stanley Shale Formation with an enlarged image (rock hammer for scale), and (b) sample AB1909 - a lamprophyre dike also intruding the Stanley Shale (human for scale). Both samples were taken from the V-intrusive dike complex, just southwest of Magnet Cove. See Figure 2a for sample locations.

puck mill and returned to the furnace for a second fusion. Major and trace element analyses were conducted at the Pomona X-Ray Fluorescence Laboratory at Pomona College with a Panalytical

Axios XRF spectrometer. Raw major element concentrations were normalized to volatile-free values, with iron expressed as Fe<sub>2</sub>O<sub>3</sub>.

### **Thick-section Analyses**

Representative portions of each sample were cut out using a diamond-tip saw and mounted in one-inch epoxy mounts which are herein referred to as “thick sections”. Mounts were cured for 24 hours then polished and gold-coated for analysis using scanning electron microscopy (SEM). Thick sections were analyzed at the Alabama Analytical Research Center (AARC) at The University of Alabama with a JEOL 7000 FE SEM equipped with an Oxford X-Max 80mm<sup>2</sup> drift detector. A working distance of 10 mm was used to maximize the efficiency of energy-dispersive X-ray spectroscopy (EDS). Accelerating voltages ranged between 15 and 20 kV with a spot size < 1 μm. EDS was primarily used to investigate the elemental composition of the samples, determine mineralogy, and corroborate XRF results. Backscattered electron (BSE) images were taken for 2-3 representative sites per thick section, and 10-20 EDS point spectra were analyzed per BSE image. EDS chemical maps of the representative sites were also used to investigate sample mineralogy.

### **Thermal Ion Mass Spectrometry (TIMS)**

Representative slices were removed from four lamprophyre samples (AB1909, AB1910, AB1912, and AB1914), ground on diamond laps to remove weathered surfaces, and pulverized using a tungsten carbide ring and puck mill. Samples were pre-contaminated by powdering a portion of sample in the mill, cleaning the mill with acetone, and powdering a second portion of the same sample in the mill a second time. 25-50 mg of the rock powders were then weighed out and spiked (200 uL/50 mg of rock) with a mixed tracer enriched in <sup>150</sup>Nd and <sup>147</sup>Sm (University of North Carolina Basalt spike: UNC “B”). Rock powders were subsequently placed in Teflon

screw cap vials and dissolved in hot HF, HNO<sub>3</sub>, and HCL. HCL was used to break down fluoride precipitates. Two-step ion chromatography was used to separate Sm and Nd. Bulk REE fractions were eluted in BioRad PolyPrep columns filled with resin and then a 2-methylactic acid (MLA) column filled with resin in order to collect Sm and Nd into separate Teflon vials. A final preparation step involves adding aqua regia to the vials containing eluted Sm and Nd, which are evaporated to remove MLA. The used method is explained in detail in Stowell et al. (2001) and Stowell and Tinkham (2003).

Sm and Nd isotopes ratios were analyzed using a VG Sector 54 thermal ionization mass spectrometer (TIMS) at the UA Radiogenic Isotope Laboratory at The University of Alabama, Tuscaloosa. Samples were loaded onto filaments which were electrically heated in the TIMS vacuum. Filaments were heated to between 1200° C and 1800° C. At these temperatures, Nd is evaporated and ionized. Ionized Nd is then accelerated by an electric field into a mass spectrometer where a large magnet separates the isotopes based on mass.

### **Paleo-stress Analyses**

Igneous dikes and other structural features for the central Arkansas region were interpreted using ArcMap software (Version 10.7.1, Esri, 2019). Shapefiles from the STATEMAP and COGEO mapping programs were provided by the AGS and downloaded for analyses. Each shapefile contains the location and extent of igneous dikes (line features) and larger igneous bodies (polygons) along with data for each feature (length and lithology). Shapefiles were combined and then divided into age groups according to the age boundaries outlined in Eby and Vasconcelos (2009), which used radiometric age data to separate AAP intrusions into three emplacement age ranges: > 100 Ma, 100-90 Ma, and < 90 Ma (Fig. 14). Approximately 340 dikes were contained in the > 100 age range and 340 dikes in the 100-90 Ma

age range. The < 90 Ma age range contains the Granite Mountain intrusion and lies primarily within the ME coastal plain. Any possible dikes in that area are likely buried by ME sedimentary fill and are thus not observed on geologic maps.

Igneous dikes are tabular bodies and were therefore treated as planar features during the analyses in ArcMap. Dike orientation or “strike” was calculated for each dike using Python code (see Appendix A). These values populated attribute tables for each age division. Attribute tables were then exported into excel for analyses on rose diagrams. Dike orientations were imported into the GeoRose program (Yong Technology Inc., 2014) to analyze any observable trends. Rose diagrams, which indicate the cardinal directions of geologic features and the number of features that follow each direction, were generated in GeoRose and are presented in Figures 14 and 15.

## RESULTS

### Major and Trace Elements

The major and trace element geochemical data for each sample area given in Table 1. Studied samples represent a wide range of SiO<sub>2</sub> (34.6-56.7 wt.%), MgO (0.3-8.9 wt.%), TiO<sub>2</sub> (0.3-6.4 wt.%), and Al<sub>2</sub>O<sub>3</sub> (6.9-21.8 wt.%) contents. Seven samples demonstrate significantly high silica contents ( $\geq 76$  wt.%), which are indicative of a non-igneous origin. Those samples are therefore not discussed in terms of igneous petrogenesis. The remaining samples plot in the alkaline series field on a total alkalis-silica (TAS) diagram (Fig. 7), and vary between ijolites, phono-tephrite, tephriphonolite, and nepheline syenite. A broad correlation between SiO<sub>2</sub> and alkali content is evident on the TAS diagram (Fig. 7). On a K<sub>2</sub>O versus Na<sub>2</sub>O diagram (Fig. 8), 7 samples plot in the shoshonitic or potassic field ( $0.5 < K_2O/Na_2O < 2$ ) and 4 samples plot in the ultrapotassic field ( $K_2O/Na_2O > 2$ ), with three of those samples – AT001, GPS001, GPS002 - having particularly high K<sub>2</sub>O contents ( $>10$  wt.%). Na<sub>2</sub>O contents of the samples vary significantly (0.9-5.3 wt.%).

On an AFM ternary diagram (Fig. 9), the studied samples follow a general curvilinear trend which begins at MgO and progresses to Fe<sub>2</sub>O<sub>3</sub><sup>T</sup> and down to the alkali (Na<sub>2</sub>O + K<sub>2</sub>O) vertices, which is expected for evolving volcanic suites. These samples are in good agreement with geographic designations for the AAP placed on an AFM diagram and explained in Morris (1987). The ultramafic samples (AB1909, AB1910, AB1912, AB1914, IDB001, Jacu001, and GBI001) have

**Table 1.**

Whole-rock analyses of igneous rocks from 3 members of the Arkansas Alkaline Province, central Arkansas.

Location	V-intrusive	V-intrusive	Benton	Benton	Benton	Magnet Cove					
Sample	AB1909	AB1910	AB1912	AB1914	IDB 001	AT 001	Cook 001	GBI 001	GPS 001	GPS 002	Jacu 001
wt. %	Lamprophyre					Phonolite		Syenite			
SiO <sub>2</sub>	40.11	39.86	37.93	40.08	35.55	53.43	48.08	34.57	56.70	55.59	36.60
TiO <sub>2</sub>	6.39	5.15	4.23	4.10	4.29	2.72	2.69	3.39	0.30	0.40	5.57
Al <sub>2</sub> O <sub>3</sub>	13.08	15.83	10.89	12.51	15.74	15.12	16.09	15.63	21.85	20.81	6.93
Fe <sub>2</sub> O <sub>3</sub>	18.81	17.66	15.06	15.85	17.44	10.21	10.92	16.71	5.04	6.29	18.01
MnO	0.55	0.28	0.25	0.15	0.28	0.26	0.26	0.34	0.45	0.43	0.29
MgO	4.47	5.04	8.13	7.89	7.94	2.54	2.70	5.58	0.30	0.33	8.98
CaO	9.02	9.94	17.50	13.14	12.39	1.86	8.51	16.44	0.57	1.07	19.97
Na <sub>2</sub> O	3.05	1.60	1.75	2.07	0.48	0.99	5.30	3.59	2.66	2.80	1.31
K <sub>2</sub> O	2.26	2.30	2.78	2.53	4.59	10.80	4.21	2.03	11.45	11.38	0.72
P <sub>2</sub> O <sub>5</sub>	1.55	1.66	0.87	0.83	0.81	1.38	0.57	1.06	0.06	0.08	1.18
Total	99.28	99.31	99.40	99.17	99.50	99.31	99.34	99.33	99.36	99.19	99.57
ppm											
Rb	72.9	103.9	98.7	76.3	148.2	222.1	122.6	82.5	535.5	506.3	20.0
Sr	1333.7	1372.0	1242.8	1112.9	488.0	715.4	1746.9	2314.6	828.8	1498.4	607.3
Ba	1313.7	1385.6	1635.5	4011.2	1379.1	3334.3	1838.3	1261.2	3067.9	3703.6	303.2
Zr	664.2	491.3	288.7	315.4	336.6	239.5	403.8	45.8	238.1	249.6	307.2
Y	44.4	46.2	22.3	30.5	33.8	32.7	45.2	39.7	9.2	13.3	37.0
Nb	313.6	240.4	159.2	109.9	143.8	188.3	206.9	266.9	169.6	209.7	173.1
Mo	3.2	-	-	3.1	3.3	2.0	6.0	2.0	46.0	26.6	9.0
Cs	264.0	145.9	43.5	105.8	17.4	-	14.1	-	-	-	-
Sc	13.7	12.6	41.4	32.6	34.9	4.1	9.0	5.1	-	-	35.0
V	676.9	659.2	469.1	469.0	503.3	360.2	286.3	989.2	99.1	133.0	510.3
Cr	12.7	18.9	74.3	36.6	43.6	55.3	-	-	9.2	35.8	290.1
Ni	28.5	27.3	56.3	87.5	92.6	32.7	18.1	14.3	10.2	15.3	90.0
Cu	121.4	130.2	180.4	115.0	175.4	222.1	54.2	69.3	24.5	28.6	117.1
Zn	209.1	186.8	99.8	122.1	111.1	137.1	147.7	97.8	156.4	199.4	113.1
Ga	31.7	28.3	19.1	20.3	28.3	20.5	24.1	21.4	25.5	22.5	20.0
La	147.8	158.5	99.8	97.7	111.1	52.2	135.6	58.1	68.5	82.8	153.1
Ce	296.7	338.0	200.6	179.0	214.6	90.1	264.2	99.8	107.3	107.4	321.2
Pr	32.7	34.6	23.3	20.3	25.1	12.3	29.1	13.2	14.3	17.4	33.0
Nd	130.9	145.9	92.3	83.4	90.4	35.8	103.5	29.5	20.4	24.5	137.1
Hf	15.8	12.6	10.6	8.1	12.0	4.1	9.0	-	-	-	8.0
Ta	18.0	16.8	13.8	8.1	6.5	6.1	8.0	-	-	4.1	15.0
Pb	11.6	5.2	-	12.2	10.9	9.2	13.1	-	21.5	23.5	4.0
Th	29.6	28.3	22.3	14.2	27.2	23.5	20.1	5.1	12.3	14.3	28.0
U	-	-	-	-	-	4.1	5.0	7.1	12.3	11.3	5.0

**Table 2.**

Whole-rock Nd isotopic composition of AAP lamprophyres.

Location	V-intrusive	V-intrusive	Benton	Benton
Sample	AB1909	AB1910	AB1912	AB1914
Sm (ppm)	20.94	20.13	8.93	21.24
Nd (ppm)	129.32	127.96	55.98	126.50
Sm/Nd	0.161953	0.157345	0.159545	0.167925
<sup>147</sup> Sm/ <sup>144</sup> Nd	0.097914	0.095128	0.096457	0.101524
( <sup>143</sup> Nd/ <sup>144</sup> Nd) <sub>i</sub>	0.512734	0.512732	0.512663	0.512648
±2σ	0.000024	0.000024	0.000024	0.000024
εNd(t)	4.37	4.32	2.94	2.66
T <sub>DM</sub> (Ma)	346	343	434	467

**Table 3.**

Summarized zircon (U-Th)/He age data.

Lithology	Sample	Age (Ma)	error*	U (ppm)	Th (ppm)	Th/U	He (nmol/g)	Ft
Volcanic Tuff	zAB-19-5-1	178.4	14.28	74.8	28.9	0.39	65.5	0.82
	zAB-19-5-2	212.6	17.01	98.4	58.0	0.59	111.8	0.86
	zAB-19-5-3	128.5	10.28	15.4	26.7	1.74	13.0	0.86
	zAB-19-6-1	192.0	15.36	85.5	96.0	1.12	93.6	0.82
	zAB-19-6-2	134.2	10.74	392.3	214.0	0.55	253.1	0.78
	zAB-19-6-3	157.1	12.57	83.7	32.3	0.39	65.0	0.83
	zAB-19-7-1	141.9	11.35	54.4	65.4	1.20	39.8	0.74
	zAB-19-7-2	186.1	14.89	129.9	73.7	0.57	107.6	0.72
	zAB-19-7-3	183.1	14.65	31.3	43.4	1.39	30.9	0.74
	Lamprophyre	zAB-19-9-1	148.8	11.90	64.4	23.7	0.37	44.9
zAB-19-9-3		168.2	13.45	69.5	40.1	0.58	52.8	0.73
zAB-19-10-1		147.0	11.76	9.1	32.6	3.59	9.6	0.71
zAB-19-10-2		175.1	14.01	53.5	23.7	0.44	42.4	0.75

\*Calculated method error

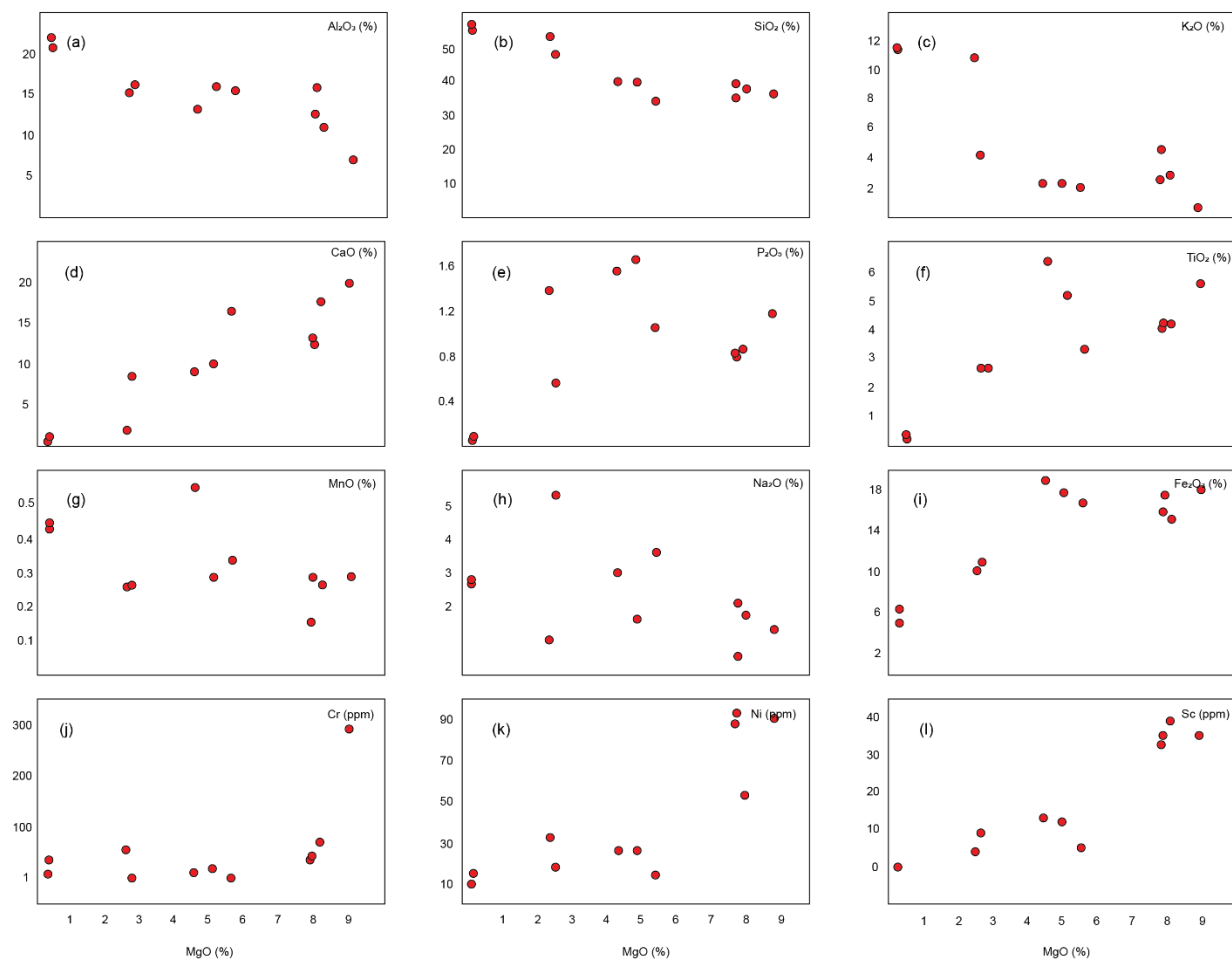


**Figure 6.** Harker plots of MgO (%) vs. (a) Al<sub>2</sub>O<sub>3</sub>, (b) SiO<sub>2</sub>, (c) K<sub>2</sub>O, (d) CaO, (e) P<sub>2</sub>O<sub>5</sub>, (f) TiO<sub>2</sub>, (g) MnO, (h) NaO, (i) Fe<sub>2</sub>O<sub>3</sub><sup>T</sup>, (j) Cr, (k) Ni, and (l) Sc.

high Fe<sub>2</sub>O<sub>3</sub><sup>T</sup> contents and thus plot the closest to the F vertices within the tholeiitic series.

Samples Cook001 and AT001 plot closer towards the alkali vertices near the calc-alkaline vs. tholeiitic discriminatory line. Syenite samples (GPS001 and GPS002) plot closest to the alkali vertices with very low MgO contents.

To fully understand the magmatic processes responsible for generation of the studied samples and identify major fractionating phases, MgO is used as an index of fractionation and plotted against specific major oxides and trace elements. A negative correlation is shown between MgO and Al<sub>2</sub>O<sub>3</sub>, while positive correlations are apparent with Fe<sub>2</sub>O<sub>3</sub> and CaO. No correlations are apparent between MgO and TiO<sub>2</sub>, Na<sub>2</sub>O, or K<sub>2</sub>O. Lamprophyre samples AB1909 and AB1910

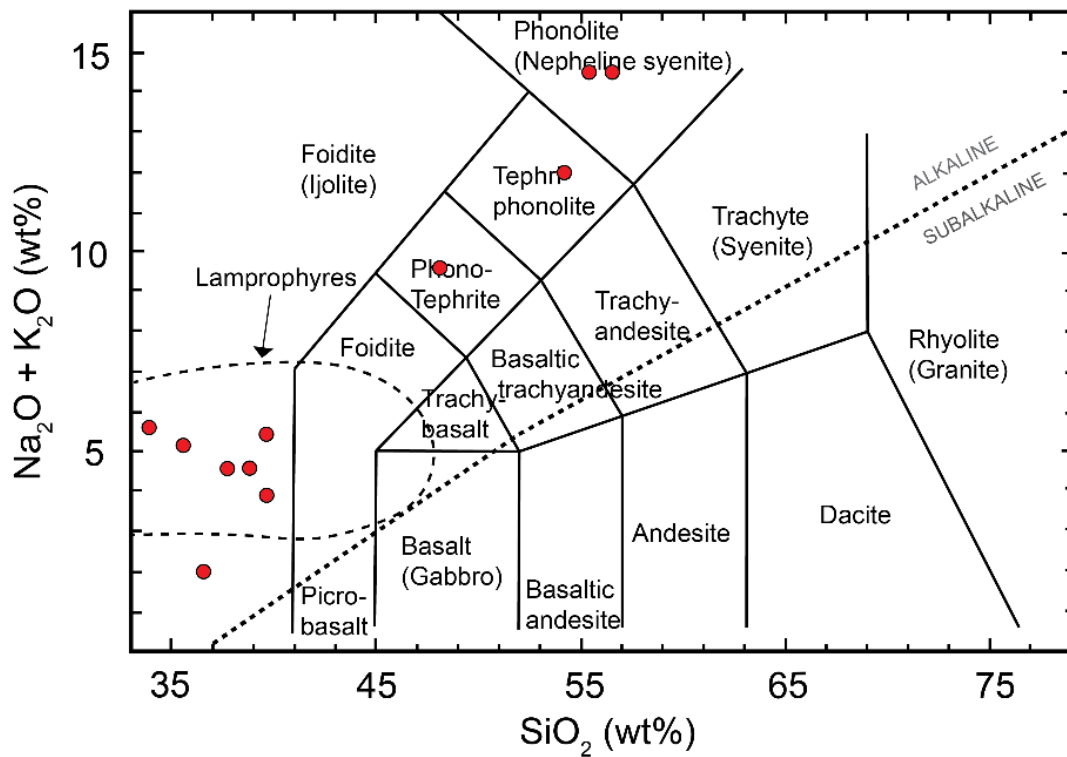


**Figure 7.** SiO<sub>2</sub> vs. (Na<sub>2</sub>O + K<sub>2</sub>O) discrimination diagram after Middlemost (1994).

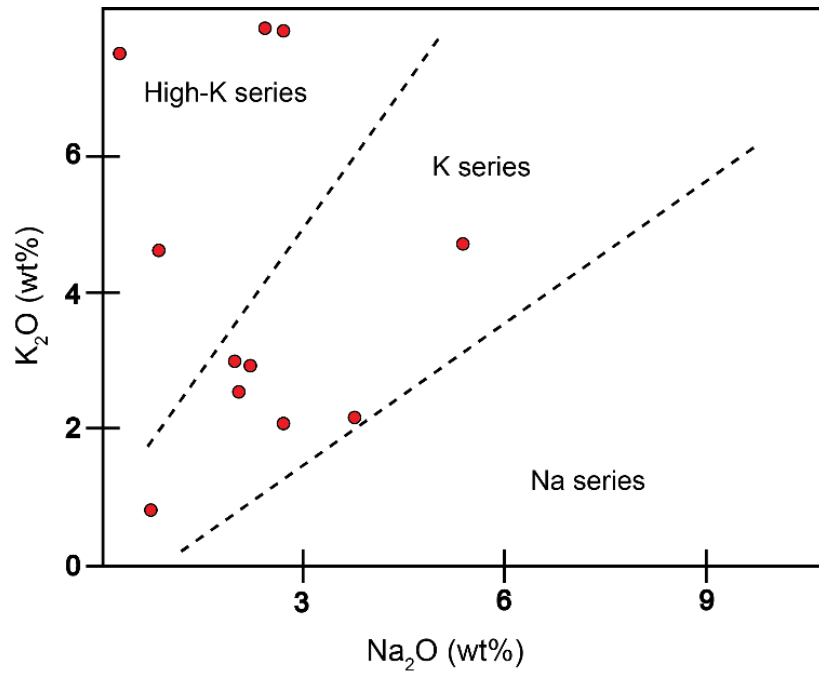


**Figure 8.**  $\text{Na}_2\text{O}$  vs.  $\text{K}_2\text{O}$  discrimination diagram (fields after Stoppa et al., 2014) that demonstrates the potassic nature of the studied samples.

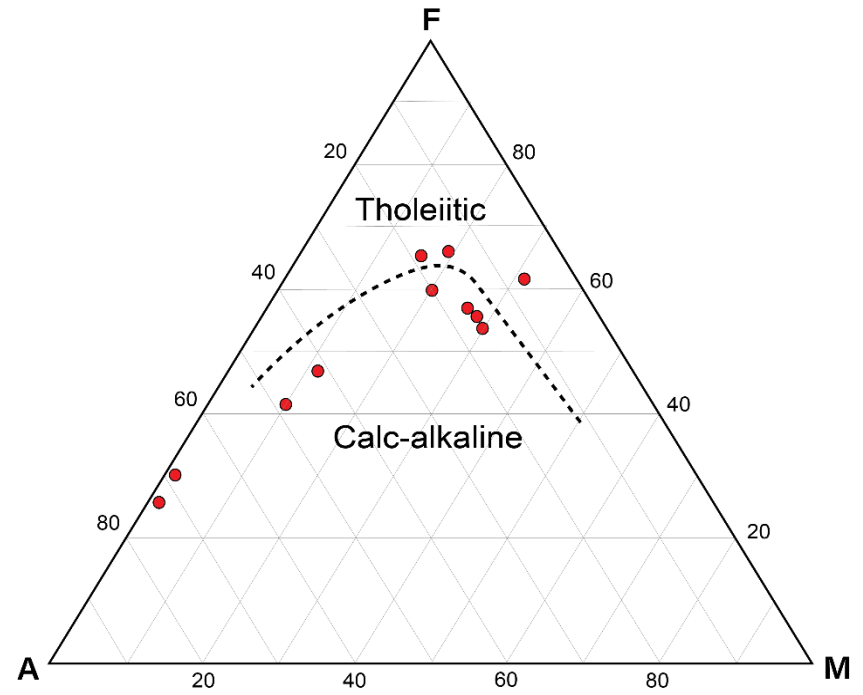


**Figure 9.** AFM diagram after Irvine and Baragar (1971), with  $A = \text{Na}_2\text{O} + \text{K}_2\text{O}$ ,  $F = \text{Fe}_2\text{O}_3^T$ , and  $M = \text{MgO}$ .

(V-intrusive) systematically exhibit lower CaO and MgO compared to AB1914 (lamprophyre – Benton Dike Swarm) at a similar SiO<sub>2</sub> content (Fig. 5b, 5d). A moderate negative correlation is evident between MgO and Al<sub>2</sub>O<sub>3</sub>. Ultramafic samples demonstrate high Al<sub>2</sub>O<sub>3</sub> contents (11-16 wt.%) except for Jacu001, which contains 6.9 wt.%. Al<sub>2</sub>O<sub>3</sub> contents are remarkably similar between ultramafic samples (AB1910, GBI001, IDB001, and Jacu001) and the higher silica syenite sample Cook001. The remaining syenite samples – GPS 001 and GPS 002 – represent the highest Al<sub>2</sub>O<sub>3</sub> contents in the dataset (21.8 and 20.8 wt.%, respectively). MnO and P<sub>2</sub>O<sub>5</sub> demonstrate no consistent trends with increasing MgO, although it is worthy to note that GPS001 and GPS 001 contain very low P<sub>2</sub>O<sub>5</sub> contents (0.06 and 0.08 wt. %).

Trace element abundances vary between samples. Compatible trace elements for samples are shown in Figures 10a-10b and range in composition: Sc = 0-39 ppm, V = 99-989 ppm, Cr = 0-290 ppm, and Ni = 10-93 ppm. The compatible element Co is below detection limits (bdl) in all 11 samples. Ni and Sc demonstrate broad correlations ( $R^2 = 0.68$  and  $0.84$ , respectively) with MgO contents. There is no apparent correlation between Cr and MgO. Two samples – Cook001 and GBI001 – contain no Cr, while sample Jacu001 represents the highest Cr content in the dataset with 290 ppm.

Trace element diagrams are shown in Figure 10 (a-f) and are discussed separately according to sample lithology and province to provide clarity. Primitive mantle normalized trace element spider diagrams for the samples are shown in Figure 10a. On a primitive mantle-normalized diagram, lamprophyre samples (AB1909, AB1910, AB1912, AB1914) are enriched in incompatible elements including high field-strength elements (Zr, Hf, Nb, Ta), and especially so in large-ion lithophile elements (LILEs) (Rb, Sr, Ba) (Fig. 10b-c). A strong U anomaly is present in sample AB1914 but not in the remaining lamprophyre samples, which exhibit U

contents below detection limits. Lamprophyres also exhibit a strongly negative Pb anomaly, as expected.

Similar to the lamprophyres, the phonolite sample (AT001) demonstrates a strongly positive U anomaly and a less-significant Pb anomaly (Fig. 10a). The phonolite exhibits extreme enrichment in incompatible elements, especially the LILEs. HFSE enrichment is present in Nb, Ta, and U, but less so in Zr and Hf, with a negative Th anomaly. The syenite samples (Cook001, GPS001, GPS002) show strong enrichment in LILEs, a positive U anomaly, and a negative Pb anomaly. Samples GPS001 and GPS002 lack Ta and Hf contents and demonstrate Y contents only 2x that of primitive mantle (Fig. 10a).

The jacupirangite sample (Jacu001) exhibits lesser enrichment in LILEs compared to other samples yet a negative Sr anomaly. Positive anomalies are present in light rare earth elements (LREE) Pr, Nd, and Sm. The ijolite sample (GBI001) reveals a positive Sr anomaly, with multiple trace elements – Th, Ta, Pb, Hf – below detection limits (Fig. 10a).

Trace element data for each sample are also normalized to average values for MORB (Sun and McDonough, 1989) and shown in Figure 10 d-f. On this diagram, LILEs (Rb, Ba) are plotted on the far left and HFS elements are plotted along the rest of the axis towards the right of the diagram. The incompatibility of elements increases towards the left-center of the diagram (at Ba and Th). Average OIB values (Sun and McDonough, 1989) are also plotted for comparison. Lamprophyre samples (AB1909, AB1910, AB1912, and IDB001) demonstrate a gentle arched pattern at Ba-Th and a generally smooth negative slope, similar to the OIB (Fig. 10e-f). However, lamprophyres are enriched (compared to OIB) in most elements except where AB1912, Cook001, and IDB001 exhibit similar amounts of Zr, Hf, Sm, and Y. The remaining lamprophyre sample – AB1914 – is distinguished by a strong Ba peak (Fig. 10e).

Syenite samples GPS 001 and GPS 002 demonstrate a similar pattern, with broadly negative slopes and much higher enrichment in incompatible elements compared to average OIB values and even higher enrichment compared to MORB (Fig. 10d). HFS elements are the most enriched in the syenites on the order of 1000x MORBS for Rb. Syenites demonstrate the most similarity with OIB trace element contents from the center of the diagram to the right (Ce-Y), except for Hf which is bdl for both samples. The phonolite sample (AT001) demonstrates similar

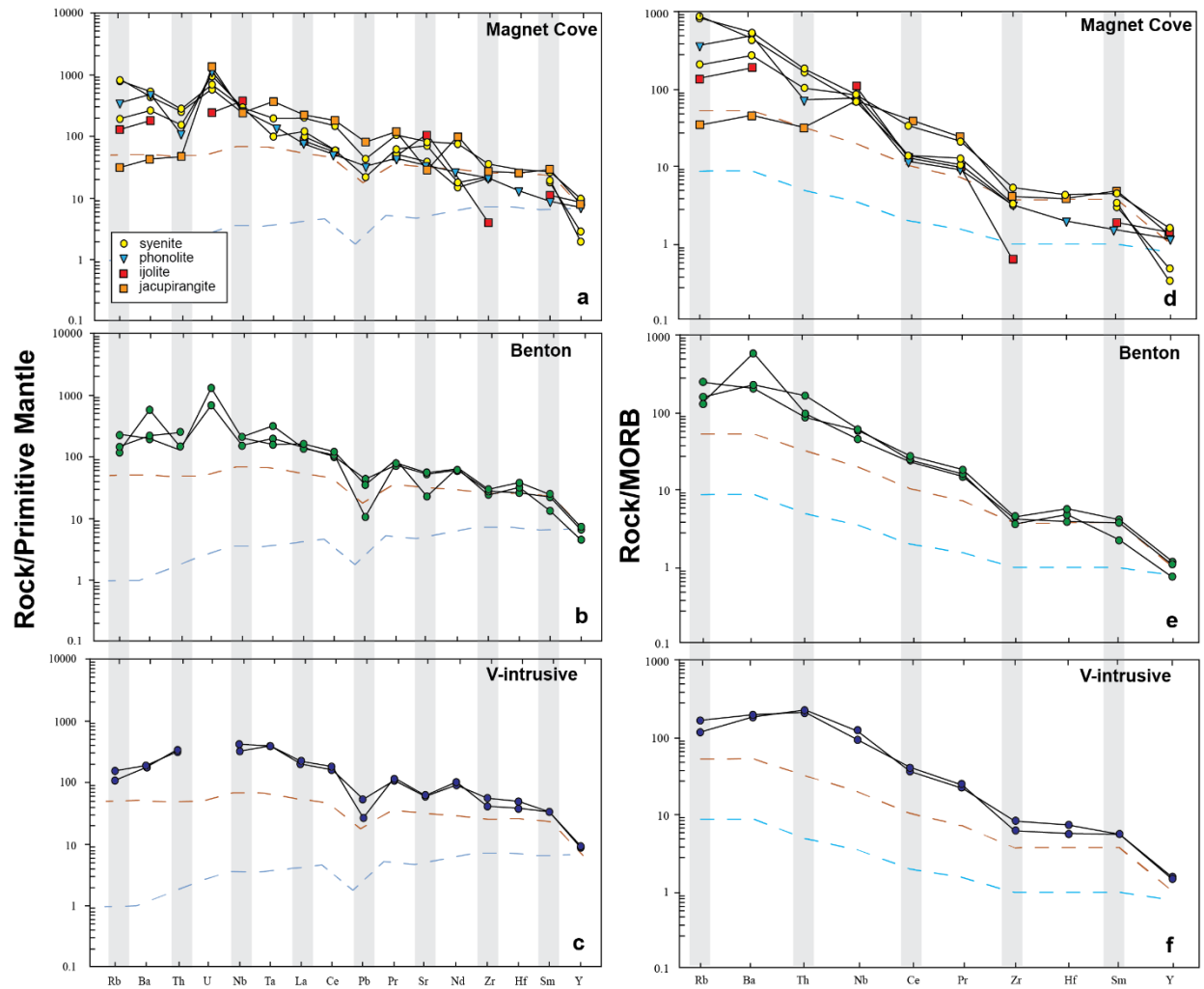


**Figure 10.** Trace element spider diagrams normalized to primitive mantle and MORB values after Sun and McDonough (1989). Trace element abundances are normalized and separated by AAP province. OIB values are given by an orange dashed line and EMORB values are given by a blue dashed line.

enrichment compared to the syenites but is characterized by positive anomalies at Ba and Nb, and a negative anomaly at Th (Fig. 10d). Trace element contents for the phonolite intersect OIB values at Zr and are lower than OIB averages for HFS element Hf and REE Sm and Y.

Certain incompatible trace element ratios (TERs) (Ce/Pb, Nb/U, and Ba/Rb) are known to remain constant throughout magmatic evolution and are thus referred to as “canonical” ratios in the literature (see Workman and Hart, 2005 and references therein). The constancy of these ratios is interpreted to be due to bulk partition coefficients that are nearly the same for each pair of elements during upper mantle melting, which prevents noticeable fractionation. Thus, these ratios are presumed to be similar between the melt and the source.

Due to their presumed constancy during melting, canonical TERs are employed in this study to identify the sources from which they were derived. Ce/Pb, Nb/U, Ba/Rb, and Rb/Sr ratios are plotted against published values from the literature in Figures 11 and 12 and discussed below. Ce/Pb ratios for nine of the studied samples vary between 21.4-94.5, while the other two samples yield undefined Ce/Pb ratios due to bdl Pb contents. These ratios are quite scattered in comparison to published Ce/Pb values of 20 and 25 (see Workman and Hart, 2005 and references therein) although the average (30.6) is only slightly higher than the uniform value of  $25 \pm 5$  for both MORBs and OIBs published in Hofmann et al. (1986). In Figure 11a, sample Ce/Pb ratios are plotted alongside the MORBs and OIBs average Ce/Pb values (Hoffman et al., 1986), average PM (Sun and McDonough, 1989), and average continental crust (Rudnick and Gao 2003) for comparison. Sample ratios plot to the right of the diagram with four of the samples within or bordering the MORB and OIB field. One ratio is slightly lower ( $\sim 14.6$ ) than the MORB-OIB minimum boundary line and the remaining four are higher than the maximum

bounding line. Lamprophyre samples AB1910 and AB1912 exhibit the highest Ce/Pb ratios with 64.4 and 94.5, respectively.

Nb/U ratio values for the samples exhibit significant variation between 5.28 and 52.4, with three of the lamprophyre samples (AB1909, AB1910, and AB1912) yielding no ratios due to bdl U contents. The average ratio (14.8) for the samples is significantly lower than the average ratio of  $47 \pm 10$  taken from a suite of oceanic basalt data published in Hofmann et al. (1986) and discussed in Sims and DePaolo (1997). Figure 11b indicates that Nb values for the samples do not vary significantly and thus scatter in Nb/U ratios is primarily controlled by differing amounts of U in the samples, which is known to be mobile during alteration and/or rock-fluid interaction (Dawood et al., 2003). The majority of ratios interestingly plot well below the minimum boundary line (37) for average MORB-OIB Nb/U ratios, and exhibit similar ratios to average continental crust after Rudnick and Gao (2003) but higher amounts of Nb. GBI001 is the only sample in this dataset with a Nb/U ratio that plots near the average MORB-OIB boundary lines, with a ratio of 52.4.

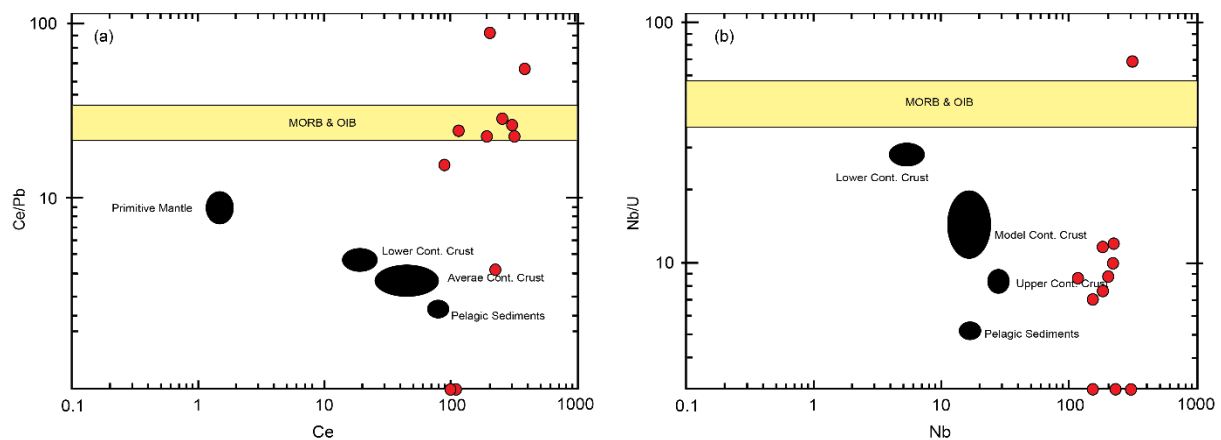


**Figure 11.** Trace element ratio diagrams for the studied samples including (a) Ce vs. Ce/Pb and (b) Nb vs. Nb/U. Plots and average values for MORB & OIB, continental crust, pelagic sediments, and primitive mantle are from Sims and DePaolo (1996) and references therein.

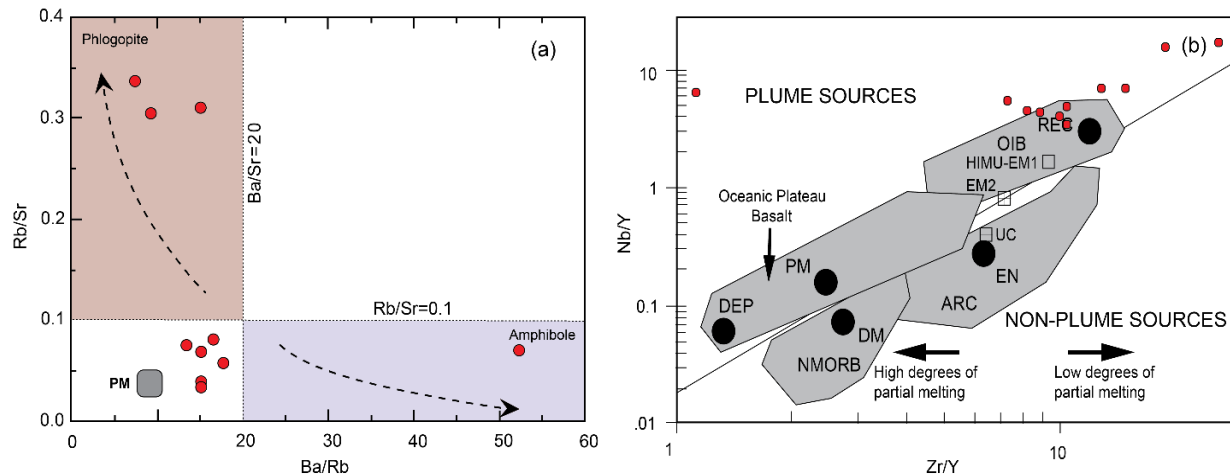


**Figure 12.** Trace element ratio diagrams for the studied samples including (a) Ba/Rb vs. Rb/Sr after Ma et al. (2014) and (b) Zr/Y vs. Nb/Y after Baksi (2001).

Ba/Rb and Rb/Sr ratios are variable for the samples (5.7-52.6 ppm and 0.03-0.6 ppm, respectively) (Fig. 12a). Ten samples have lower Ba/Rb (< 20) while a single lamprophyre sample (AB1914) has a very high Ba/Rb of 52.3. On a Ba/Rb vs. Rb/Sr diagram (see e.g. Furman and Graham, 1999; Ma et al., 2013), six of the lower Ba/Rb samples plot near average primitive mantle Rb/Sr and Ba/Rb values (Sun and McDonough, 1989) (Fig. 12a). Three low Ba/Rb samples (AT001, GPS002, and IDB001) plot in the phlogopite source field, while the higher Ba/Rb sample (AB1914) plots in the amphibole source field.

Fitton et al. (1997) initially suggested that a deep depleted mantle source can be distinguished from a shallow MORB source using the trace element ratios Zr/Y and Nb/Y. Baksi (2000) supported this hypothesis by plotting mafic lavas derived from the Icelandic plume on multiple Nb-Y-Zr plots. The same plot is used for this study and shown in Figure 12b. Zr/Y and Nb/Y sample ratios are plotted against average mantle compositional components (enriched mantle, depleted mantle, primitive mantle, and recycled component) and various tectonic settings (oceanic plateau, NMORB, subduction, volcanic arc, and OIBs) (Weaver, 1991; Condie, 2003). Each of the sample Nb/Y ratios plot above the  $\Delta$ Nb line that discriminates between plume

and non-plume sources. The majority of samples plot to the far right of the diagram, with four samples plotting within the bounds of the OIB polygon and near the recycled component (REC). Four more samples plot just outside the bounds of the OIB polygon. Syenite samples GPS 001 and GPS 002 represent the highest Zr/Y ratios (25.9 and 18.8, respectively) and the highest Nb/Y ratios (18.4 and 15.8, respectively). Sample GBI001 (Nb/Y = 6.7, Zr/Y = 1.2) interestingly plots to the far left of the diagram nowhere near compositional components or tectonic settings.

### **Nd Isotopic Geochemistry**

Whole-rock Nd for four lamprophyre samples are listed in Table 2. Nd and Sm data are normalized to  $^{146}\text{Nd}/^{144}\text{Nd} = 0.7219$  and  $^{149}\text{Sm}/^{152}\text{Sm} = 0.51685$ , respectively. Lamprophyre samples demonstrate a range of values for the Sm-Nd system, with  $^{147}\text{Sm}/^{144}\text{Nd}$  values between 0.095128 and 0.101524 and more consistent  $^{143}\text{Nd}/^{144}\text{Nd}$  values (0.512663 – 0.512798). Initial  $^{143}\text{Nd}/^{144}\text{Nd}$  values define a range between 0.512648 and 0.512734. The lamprophyres yield positive  $\epsilon\text{Nd}$  values between +2.66 and +4.37 and depleted mantle model ages ( $T_{\text{DM}}$ ) of 346 – 467 Ma. Isotopic ratios are plotted against published data for other AAP members and mantle end members including enriched mantle (EMI, EMII), depleted mantle (DM), bulk silicate earth (BSE), and primitive helium mantle (PHEM) (Fig. 13).

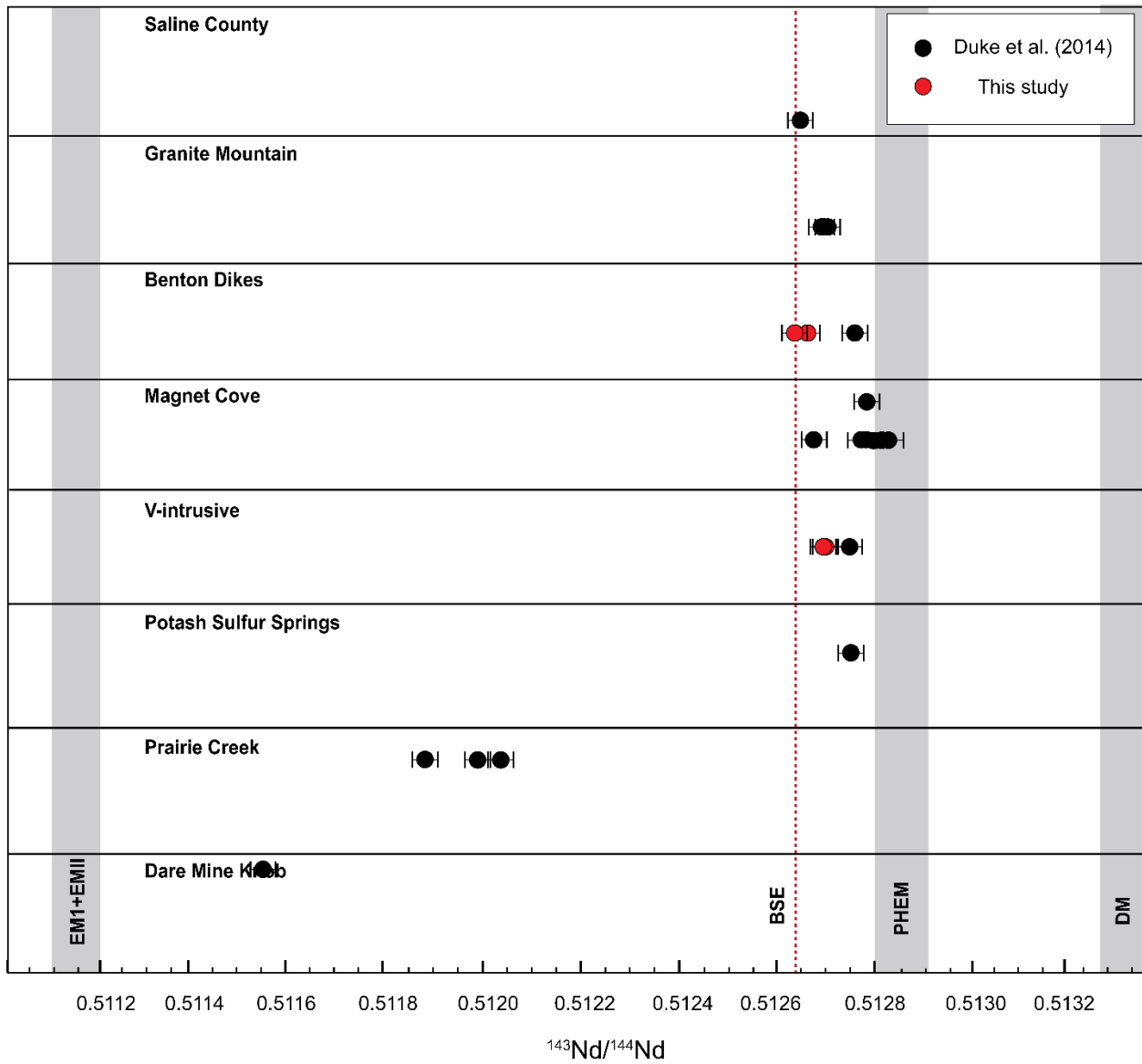


**Figure 13.** Initial  $^{143}\text{Nd}/^{144}\text{Nd}$  isotopic ratio plots for all eight provinces of the AAP. Various mantle reservoirs – EMI, EMII, PHEM, and DM – are plotted for comparison (EMI, EMII, DM, BSE – Rollinson, 1993; PHEM – Farley et al., 1992). Values from Duke et al. (2014) are also plotted alongside data produced in this study.

## **(U-Th)/He Results**

Zircon single grain (U-Th)/He data are reported in Table 3 for six of the 21 studied samples. Three zircon crystals from sample AB1905 yielded ZHe ages ranging from 128.5 to 178.4 Ma with an average age of 173.2 Ma. Three zircon crystals from sample AB1906 yielded ZHe ages ranging from 134.2 to 192.0 Ma with an average age of 161.1 Ma. Three zircon crystals from sample AB1907 yielded ZHe ages ranging from 141.9 to 186.1 Ma with an average age of 170.3 Ma. ZHe ages are also reported for two lamprophyre samples in Figure 4: AB1909 and AB1910. Two zircon crystals from sample AB1909 yielded ages ranging from 148.8 to 168.2 Ma with an average age of 158.5 Ma. Two zircon crystals from sample AB1910 yielded ages ranging from 147.0 to 175.1 Ma with an average age of 161.1 Ma.

Th/U ratios for the zircons are also reported in Table 3. Samples AB1905, AB1906, and AB1907 range between 0.39 and 1.74, with an average Th/U = 0.88. The lamprophyre samples (AB1909 and AB1910) demonstrate Th/U values between 0.37 and 3.59 with an average Th/U = 1.25. Due to the possibility of inheritance and partial resetting of these grains from the host rock, we interpret these dates as maximum emplacement ages. Due to a low silica content and relatively low Zr content it remains unclear if sampled dikes reached Zircon saturation and crystallized zircon. If the youngest ages are in fact emplacement ages, then this would argue against any sort of age progression identified previously.

## **Petrography**

Based on SEM thick section imaging and EDS analyses, the discussed samples can be divided into four primary groups: lamprophyre, ijolite, jacupirangite, and syenite. Mineral assemblages are typical for each lithology and are discussed in the following sections. The lamprophyres are fine to coarse grained with a hypocrySTALLINE porphyritic and panidiomorphic

texture. Mineralogy of the lamprophyres varies, as one sample (AB1914) contains forsteritic olivine and the remaining four are olivine-free. Common minerals among every lamprophyre are

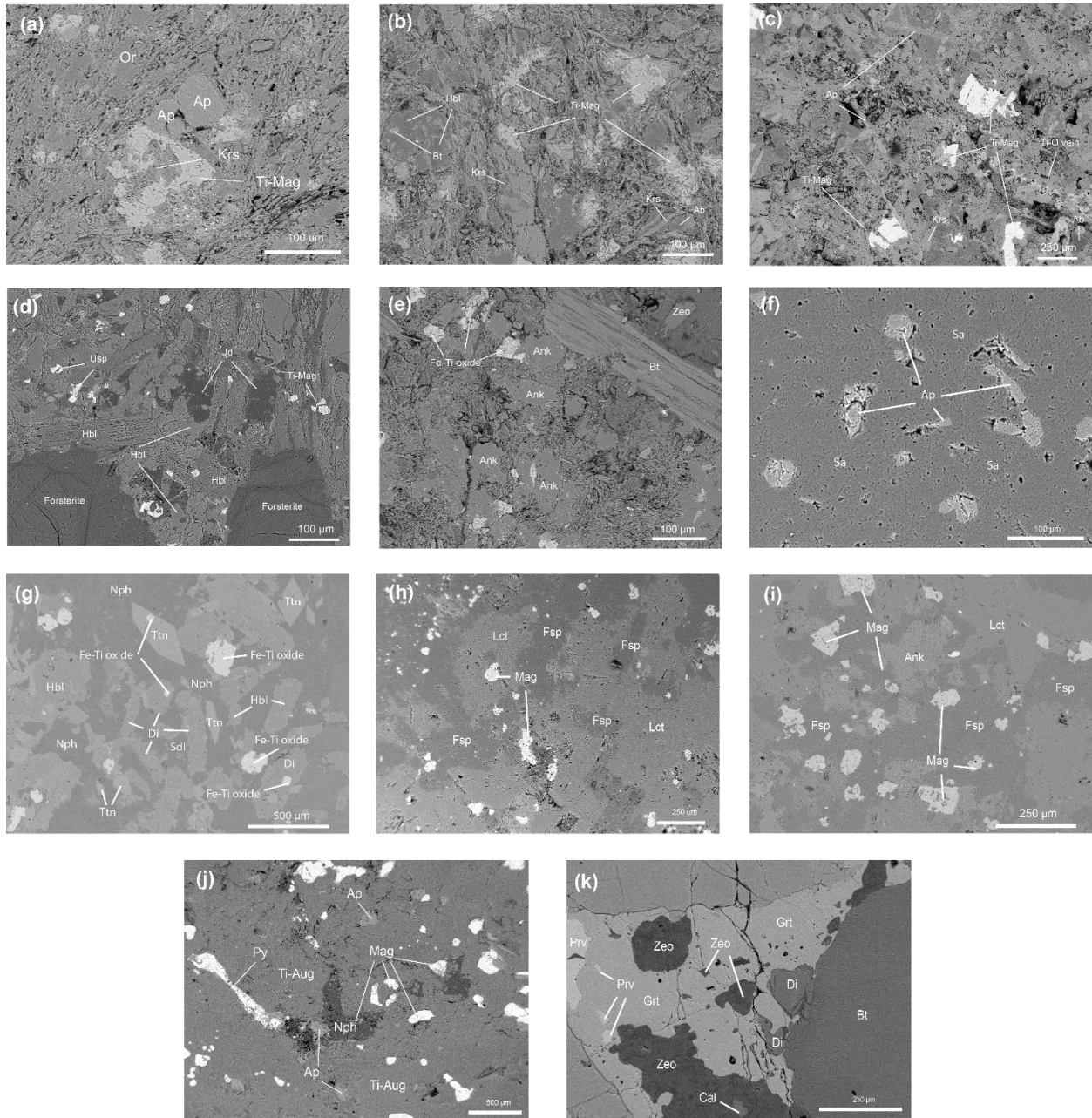


**Figure 14.** Backscattered electron images of eleven samples: (a) AB1909, (b) AB1910, (c) AB1912, (d) AB1914, (e) IDB001, (f) AT001, (g) Cook001, (h) GPS001, (i) GPS002, (j) Jacu001, and (k) GBI001. Ab – albite; Ank – ankerite; Ap – apatite; Aug – augite; Bt – biotite; Cal – calcite; Di – diopside; Fsp – Feldspar; Grt – garnet; Hbl – hornblende; Jd – jadeite; Krs – kaersutite; Lct – leucite; Mag – magnetite; Nph – nepheline; Or – orthoclase; Prv – perovskite; Sa – sanidine; Scl – sodalite; Ttn- titanite; Usp – ulvospinel; Zeo – zeolite.

amphibole and abundant Fe-Ti oxides.

Lamprophyre samples from the V-intrusive are mineralogically similar with phases including euhedral to subhedral apatite, subhedral to anhedral Fe-Ti oxides (titanomagnetite and ulvospinel), subhedral amphibole (kaersutite and hornblende), subhedral plagioclase feldspar, and minor amounts of biotite (Fig. 14a-b). Fe-Ti oxides are poikilitic with smaller amphibole inclusions. Biotite occurs primarily as microphenocrysts and inclusions in feldspar. The matrix of these samples is comprised of plagioclase, amphibole and Ti-oxides. Based on their mineral assemblage, these olivine-free lamprophyres are classified as camptonites (Rock, 1991).

Lamprophyres from the Benton Dike Swarm (AB1912 and IDB001) differ mineralogically from one another and from the discussed V-intrusive samples (Fig. 14c, e). Sample AB1912 is characterized by subhedral amphibole (kaersutite), subhedral Fe-Ti oxides, euhedral apatite phenocrysts, subhedral plagioclase and alkali feldspar, subhedral rutile, and minor amounts of subhedral biotite, hauyne, and pyrite. Fe-Ti oxides and orthoclase are the largest phenocrysts and vary in diameter between 50 and 400  $\mu\text{m}$ . Apatite is represented by large (500  $\mu\text{m}$ ) bladed phenocrysts that exist as inclusions within feldspar and form radial nests (not shown). Rutile occurs as phenocrysts and is concentrated in a hydrothermal vein (Fig. 14c). Feldspar occurs in the groundmass. Sample IDB001 is characterized by subhedral Fe-Ti oxides (ulvospinel and titanomagnetite), large (>200  $\mu\text{m}$ ) euhedral biotite laths, anhedral ankerite, and minor subhedral zeolite (thomsonite) and pyrite. Biotite and Fe-Ti oxides are the primary phenocrysts. Interstitial feldspar is present within the biotite laths. The groundmass is comprised primarily of feldspar and minor amounts of zeolite. According to their mineral assemblages, these samples are classified as ouachitite (IDB001) and sannaite (AB1912) (Rock, 1991).

Sample AB1914 is characterized by euhedral forsteritic olivine phenocrysts (>300  $\mu\text{m}$ ), euhedral hornblende, subhedral pyroxene, Fe-Ti oxides (ulvospinel and titanomagnetite), and minor amounts of subhedral phlogopite, euhedral pyrite, and euhedral apatite. The groundmass is comprised of minerals similar to the phenocrysts. Fe-Ti oxides and biotite are found as inclusions in pyroxene. Forsteritic olivine is abundant throughout the rock and is crosscut with iddingsite veins. Carbonate veins are also present in the rock and cut through amphibole, but not olivine. This sample is classified as a monchiquite according to the classification scheme of Rock (1991).

The remaining six samples were collected from the Magnet Cove intrusive body (see Fig. 2b) and are discussed in terms of their mineralogy and petrographic characteristics in the following sections. These samples vary in lithology between jacupirangite, ijolite, phonolite and syenite. The ijolite sample – GBI001 – was collected from the interior of the Magnet Cove (Fig. 3b). This sample is holocrystalline porphyritic with mostly anhedral grains. Minerals include anhedral masses of zeolite (thomsonite), biotite partially altered to phlogopite, clinopyroxene, and melanite garnet. Smaller amounts of subhedral perovskite, Fe-Ti oxides, and pyrite are also present in the rock. Zeolite is commonly formed through alteration of nepheline (Erickson and Blade, 1963). Pyrite and laths of mica occur as inclusions within zeolite. Subhedral calcite is also present as inclusions within zeolite. Due to its location within Magnet Cove and associated mineral assemblage, this sample is classified as a garnet biotite ijolite.

The jacupirangite sample – Jacu001 – was collected from the northeast corner of the Magnet Cove province (Fig. 3b) within the outer syenite ring, which is one of two locations within Magnet Cove where jacupirangite occurs. This sample is hypocrystalline porphyritic with euhedral to subhedral phenocrysts set in a groundmass. Primary phenocrysts include abundant

subhedral magnetite and subhedral fluorapatite, with lesser amounts of subhedral pyrite, anhedral nepheline, and fine-grained perovskite. Some pyrite and apatite phenocrysts are as large as 1 mm. The anhedral nepheline masses are poikilitic with fine grained apatite inclusions and finer magnetite inclusions. Nepheline is glomeroporphyritic, occurring in clusters and constrained to specific parts of the rock. The groundmass is primarily titanaugite.

Phonolite was sampled from the inner belt of Magnet Cove, which is primarily comprised of phonolite and trachyte. Sample AT001 is hypocrySTALLINE porphyritic and exhibits significant weathering. Euhedral to subhedral apatites are the only identified phenocrysts and are abundant throughout the rock. Apatites range in diameter from 25 to 250  $\mu\text{m}$ . The groundmass is comprised of sanidine.

Three syenite samples were collected from the Cove's outer ring, which includes varieties of feldspathoidal syenite. Samples GPS 001 and GPS 002 were sampled in close proximity and thus contain some similar characteristics. Each of these syenites is holocrystalline porphyritic, with pseudoleucite megacrysts and smaller crystals that vary between each sample. Besides the pseudoleucite crystals, GPS001 is mostly comprised of anhedral masses of k-feldspar and subhedral Fe-Ti oxides (magnetite and ilmenite). The feldspar is poikilitic with inclusions of Fe-Ti oxides. Minerals that occur in smaller amounts include anhedral masses of gahnite and ankerite, and spessartine-type euhedral garnet. GPS 002 contains a similar mineral assemblage but has larger amounts of ankerite and includes phases of biotite and sphalerite. Both GPS001 and GPS002 are classified as garnet-pseudoleucite syenites due to their characteristic pseudoleucite and garnet crystals.

The third syenite sample – Cook001 – was collected from the outer ring at the western edge of the Magnet Cove complex. Like the other two syenites, this sample is holocrystalline

porphyritic and characterized by euhedral sphene crystals, subhedral hornblende, euhedral to subhedral clinopyroxene, subhedral Fe-Ti oxides, and anhedral masses of nepheline and sodalite. Sphene, clinopyroxene, and hornblende represent the largest crystals in the rock with lengths that reach ~500  $\mu\text{m}$ . Both titanite and clinopyroxene are poikilitic with inclusions of Fe-Ti oxides. According to its mineral assemblage, this sample is identified as a sphene-nepheline syenite.

### **Dike Orientations**

Igneous intrusions are separated into three early Late Cretaceous age divisions (>100 Ma, between 100 Ma and 90 Ma, and < 90 Ma). Dikes mapped west of the 100 Ma boundary line are referred to as “Group 1” dikes while dikes between the 100 and 90 Ma boundary lines are “Group 2” dikes (Fig. 15). The only mapped igneous body east of the 90 Ma line is the Granite Mountain province. Thus, there is no need for a third group of dikes. Age divisions are taken from Eby and Vasconcelos (2009), which uses best ages from  $^{40}\text{Ar}/^{39}\text{Ar}$  radiometric age-dating of phlogopite grains at Magnet Cove, fission-track dating of apatite and titanite from multiple AAP members, and previously published age data that include  $^{40}\text{Ar}/^{39}\text{Ar}$  ages of Baksi (1997), K-Ar ages (Gogineni et al., 1978), and the U-Pb zircon age of Zartman and Howard (1987).

### **Group 1 Dikes**

Group 1 dikes have a maximum length of 1,764 m and a minimum length of 107 m. In particular, the NE-SW-trending dikes reach lengths of ~900 m but are more typically between 100 and 400 m. NW-SE-trending dikes generally range between 100 and 500 m, with a single dike at 1,764 m, which represents the maximum length for this dataset. Only four dikes trend E-W and have a small range in lengths between 186 and 267 m. There are no dikes west of the 100 Ma boundary line that trend exactly N-S. The majority of dikes in Group 1 trend NE-SW, with  $070^\circ$ - $075^\circ$

azimuths being the most prominent (Fig. 14a). These dikes demonstrate no preferred location and randomly lie west of the 100 Ma boundary line. Additionally, there is no apparent correlation between length and azimuth for NE-SW trending dikes.

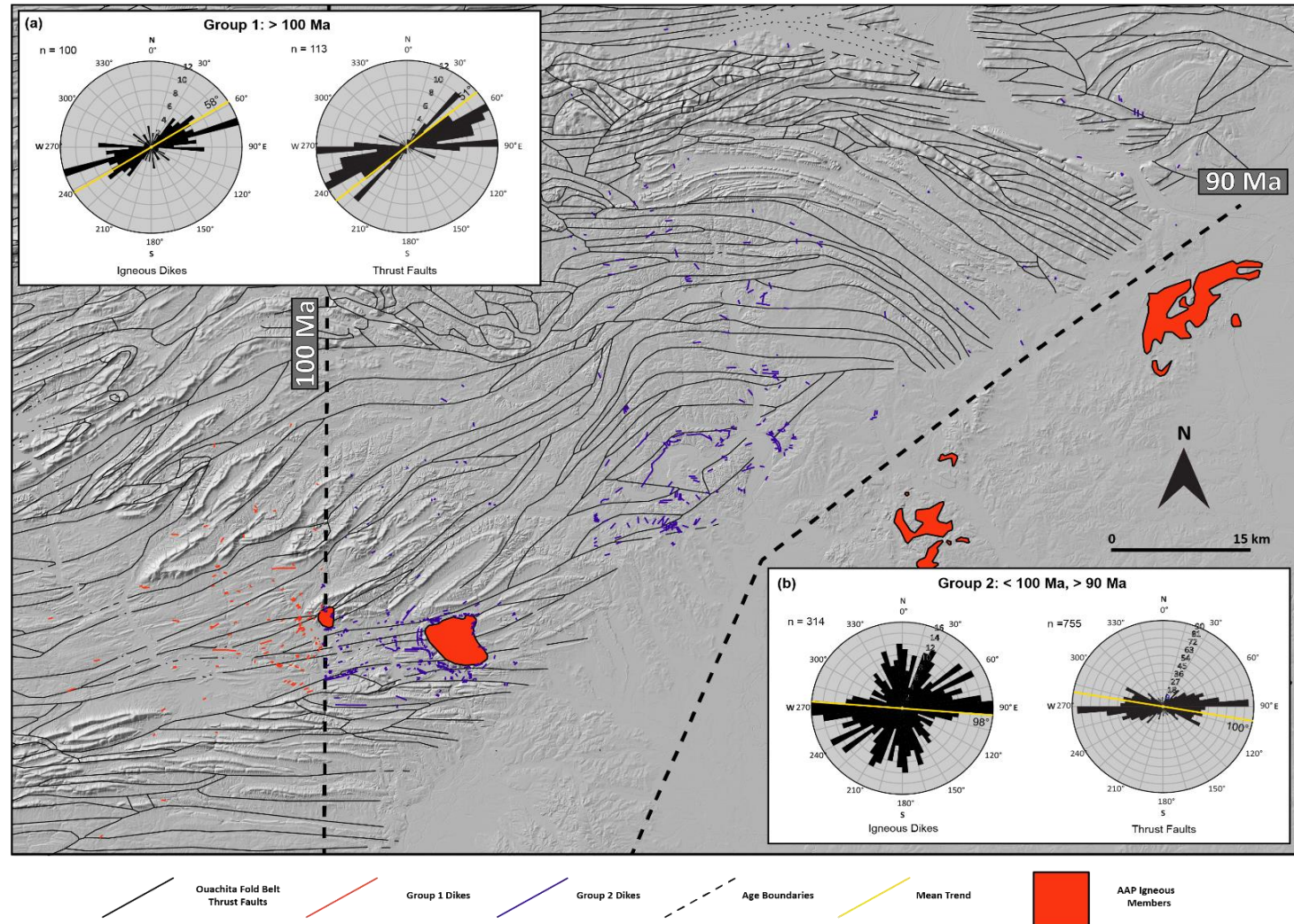


**Figure 15.** Digital elevation map of central Arkansas with overlain polygons of AAP igneous intrusions in red. Rose diagrams are shown for (a) igneous dikes great than 100 Ma in age and associated thrust faults, and (b) igneous dikes between 90 and 100 Ma in age and associated thrust faults. Mean orientations of each diagram are indicated in yellow. See Figure 1 for geographic location.

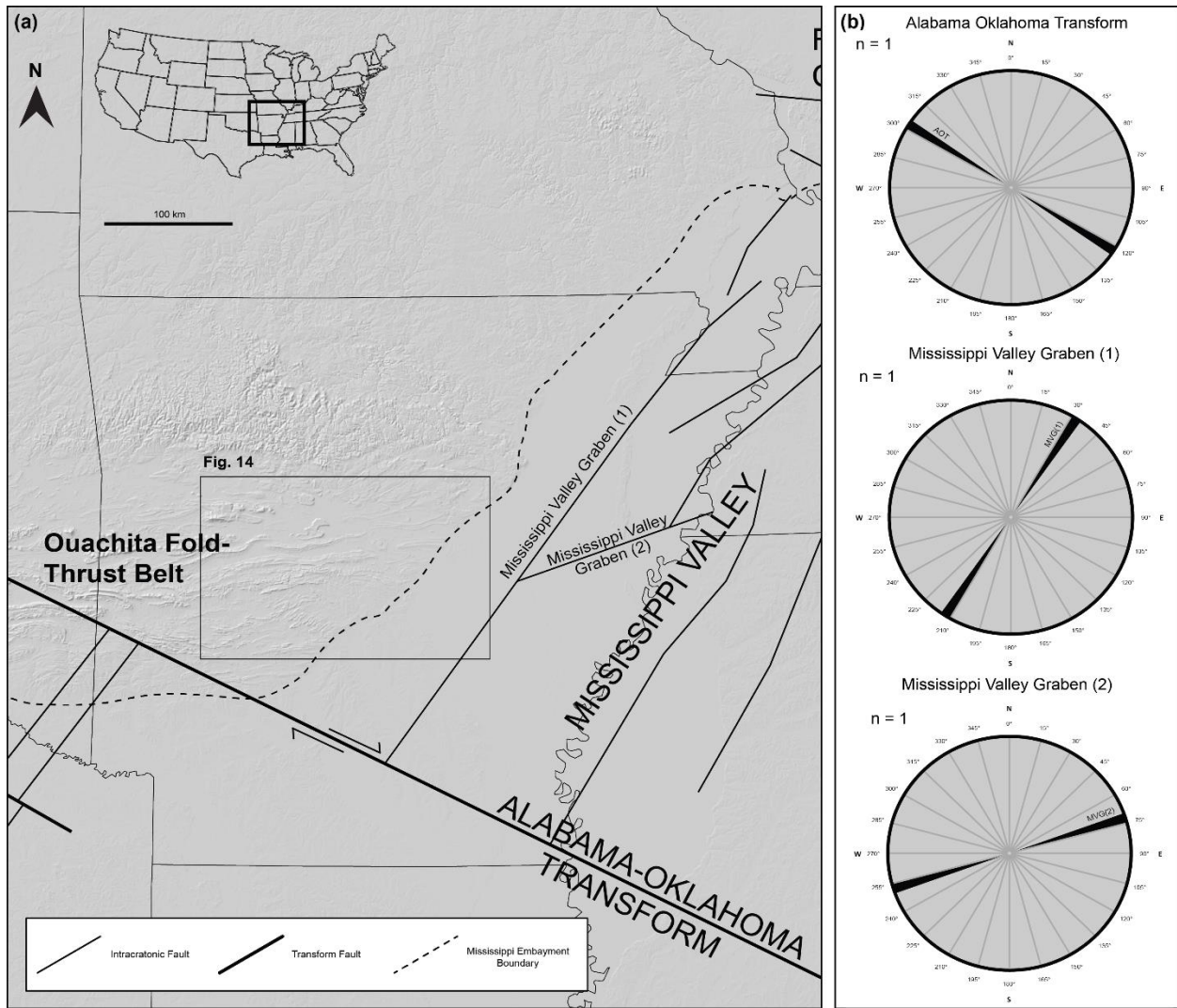


**Figure 16.** Digital elevation map of central Arkansas with basement faults (Alabama-Oklahoma Transform and Mississippi Valley Graben) shown in black and corresponding rose diagrams for individual faults shown on the right.

## Group 2 Dikes

Group 2 dikes range in length between 92 m and 5,408 m. NE-SW-trending dikes reach up to ~5,400 m in length but are generally between 90 and 1000 m in length. The NW-SE-trending dikes have a maximum length of 1,971 m with the majority of dikes ranging in length between 90 m and 1000 m, similar to NE-SW-trending dikes. Three dikes are trending exactly

N-S and demonstrate a small range in length between 116 and 222 m. Four dikes trend exactly E-W and also demonstrate a small length range between 318 and 351 m. Dikes in group 2 exhibit trends in nearly every direction, although there is a prominent trend from N085° to N095°(ENE-ESE) (Fig. 15b). There is no apparent correlation between length and azimuth for ENE-ESE-trending dikes. Although the rose diagram indicates a variety of orientations, the dikes do not follow a specific pattern of orientations. Instead, dikes of varying orientations are found sporadically in between the 90 and 100 Ma bounding lines.

### **Thrust Fault Orientations**

Thrust faults are abundant throughout the OFB and represent a segment of a Pennsylvanian-Permian thrust system formed during the Ouachita orogeny and assembly of the Pangea Supercontinent (Whitaker and Engelder, 2006). Thrust orientations in the study area are divided into groups based on the age divisions of Eby and Vasconcelos (2009) to maintain consistency with rose diagrams of dikes. Because of their proximity to dikes, orientations of thrust faults are compared with orientations of dikes to investigate the control of local, pre-existing planes of weakness on Cretaceous-age magma intrusion. Similar to the dike groupings, thrust faults west and east of the 100 Ma discriminatory line are classified as Group 1 and Group 2, respectively. Group 1 thrust faults strike primarily between 040° and 085° (NE-ENE). There are two prominent trends at 060°- 065° and 085°- 090°. This is generally consistent with Group 1 dike orientations (mean trend = 058°).

### **Basement Fault Orientations**

The orientations of basement faults – locations taken from Thomas (2014) – were calculated and compared to dike trends. These faults – MVG normal faults, and the AOT transform fault - comprise a segment of the larger Laurentian continental margin and are related

to Iapetan rifting in Late Precambrian to Cambrian time (~565-495 Ma) (Thomas, 2017). Thus, these lithospheric weaknesses existed prior to the emplacement of magmas that formed the Cretaceous-age AAP and are examined to investigate the control of pre-existing structural fabrics on dike emplacement. Faults of the MVG generally strike NE-SW and lie between south-central Arkansas and southern Illinois. Two fault segments in Arkansas lie roughly 50 km to the southeast; their orientations are roughly  $034^{\circ}$  and  $075^{\circ}$  respectively (Fig. 16b). The AOT transform fault strikes at roughly  $301^{\circ}$  (Fig. 16b).

## DISCUSSION

### Role of Partial Melting, Fractional Crystallization, and Crustal Contamination

Magmatic systems are affected by significant processes such as partial melting, fractional crystallization, and crustal contamination; these must be addressed before discussing the magma source. Trace element and major oxide geochemical data are used to investigate the influence of each process during magma evolution. Primary magmas – formed by partial melting of the upper mantle – are expected to have high Ni (400-500 ppm) and Cr (>1000 ppm) contents, with SiO<sub>2</sub> ≤ 50% (Wilson, 1989). While most of the samples analyzed during this study are silica-undersaturated, none demonstrate high Ni and Cr contents. Therefore, the samples must have developed from an evolved melt. Low degrees of partial melting are likely, suggested by extreme enrichment in incompatible elements (Figs. 10a, 10b) and high Zr/Y (Fig. 12b). This is further supported by enrichment in light-REE (Figs. 10a, 10b). Plots of compatible elements and major oxides against MgO (Fig. 6) indicate the effects of fractional crystallization. Fe<sub>2</sub>O<sub>3</sub><sup>T</sup>, CaO, and Sc all show positive correlations with MgO and thereby suggest a fractionated pyroxene phase. Ni shows a moderately positive correlation with MgO ( $R^2=0.68$ ) and could indicate fractionation of olivine. A negative correlation with MgO and Al<sub>2</sub>O<sub>3</sub> suggests that plagioclase was not an important fractionating phase. There are no apparent correlations between P<sub>2</sub>O<sub>5</sub> and MgO, indicating that apatite was not a significant fractionating phase. A weak correlation between TiO<sub>2</sub> and MgO, could indicate that Fe-Ti oxides were fractionated.

Eight of the samples demonstrate Nb/U values from 5.3-52.4 (average = 14.8), which is much lower than the canonical mantle ratio (Nb/U =  $47 \pm 10$ , Hofmann et al., 1986) and closer to

average continental crust (Fig. 11b) reflecting some crustal contamination, although the primary control on Nb/U ratios is the varying U contents, which could be determined by the mobility of U during fluid-rock interaction. Nb/U values could also be reflected by fractionation due to lower MgO contents of < 7 wt.% (Sims and DePaolo, 1997). Thus, Nb/U values must be viewed with caution. Ce/Pb ratios of the samples, on the other hand, are relatively high compared to crustal values with one sample plotting near average continental crust (Fig. 11a). Nd isotopes are also effective when determining the influence of crustal contamination.  $^{143}\text{Nd}/^{144}\text{Nd}$  values (mean  $^{143}\text{Nd}/^{144}\text{Nd} = 0.5127$ ) are significantly higher than average continental crust ( $^{143}\text{Nd}/^{144}\text{Nd} = 0.5118$ ; Hoffman, 1997), indicating little crustal contamination for the lamprophyres.

In summary, fractionation could have been an important process during magmatic evolution of the AAP, and some crustal contamination is evident. However, there is significant scatter for many elements, although some broad correlations are apparent between major oxides and trace elements. Given that the samples were collected from separate AAP outcrops, it is unlikely that the samples form a comagmatic suite.

### **Mantle Sources and Metasomatism**

Nd isotope ratios reflect the history of mantle source reservoirs (Hoffman, 1997). The isotopic dataset presented in this study represents data for dikes from two separate provinces of the AAP (the V-intrusive and the Benton Dike Swarm); these plus six remaining provinces (Fig. 3a) define the entire AAP suite. Thus, these data are discussed in unison with published geochemical data for other provinces in efforts to comprehensively understand magma sources that were potentially tapped during AAP evolution.

Nd isotopic data for the lamprophyre samples in the study area define a tight range of initial  $^{143}\text{Nd}/^{144}\text{Nd}$  values (0.512648 – 0.512734; Table 3) indicating a similar source for dikes of

the V-intrusive and Benton dikes. A mean  $^{143}\text{Nd}/^{144}\text{Nd}$  ratio of 0.512694 is in agreement with  $^{143}\text{Nd}/^{144}\text{Nd}$  ratios published for Magnet Cove carbonatites by Tilton (1987), but slightly lower than Granite Mountain syenites published in the same study. The  $^{143}\text{Nd}/^{144}\text{Nd}$  data correspond to  $\epsilon\text{Nd}(t)$  values of +2.66 to +4.37, which correspond well with carbonatite, ijolite, and jacupirangite samples Magnet Cove and Potash Sulfur Springs samples ( $\epsilon\text{Nd} = +1.9 - +4.3$ ) from Duke (2008), which are interpreted to be derived from an asthenospheric source. These values are quite different from  $\epsilon\text{Nd}(t)$  values for Prairie Creek and Dare Mine Knob (-19 to -10), which Duke (2008) suggests is indicative of a lithospheric source. Nd isotopic data are roughly similar between the V-intrusive, Benton Dike Swarm, Potash Sulfur Springs, and Magnet Cove provinces and represent mantle-derived rocks. A mantle source for samples analyzed in this study and other published AAP isotopic data is corroborated by the presence of mantle minerals (olivine, pyroxene, garnet) in the samples (Fig. 14).

Nd isotopic values demonstrate similarities to OIB-related mantle reservoirs. In comparison to other mantle reservoirs,  $^{143}\text{Nd}/^{144}\text{Nd}$  isotopic values of the lamprophyres plot closely with ratio values for some low  $^4\text{He}$  reservoirs (FOZO, PREMA, PHEM, and C) and are slightly higher than enriched mantle reservoirs (EMI and EMII), yet below average values for depleted mantle (DM) (Fig. 13). Thus, a distinct mantle end-member source for the lamprophyres is not clear. However, trace element spider diagrams normalized to primitive mantle indicate extreme enrichment in incompatible elements for the lamprophyres (Figs. 10a, 10b) indicating some enriched component in the source. Enrichment is especially evident in LILEs (Rb, Ba, and Sr) and some HFSE's (Th, U, Ce, Nb) (Figs. 10a, 10b). On MORB-normalized spider diagrams, the lamprophyres are more enriched with respect to an average MORB and demonstrate a smooth slope similar to that of an average OIB (Sun and McDonough,

1989), with common OIB indicators such as strongly negative Pb anomalies and enrichment in both HFSE and LILEs (Fig. 10b).

Given that Nd isotopic data is only presented for the lamprophyre samples, genesis of the remaining lithologies will be determined via trace element ratios and spider diagram plots. Besides ratios of Nd isotopes, ratios of incompatible trace elements are also useful for fingerprinting the magmatic origin of the studied samples. Specific TERs are used due to their constancy during magma evolution. Figures 11 and 12 shows plots for a variety of TERs for the studied samples. In particular, Zr/Nb ratios for the samples are relatively low ( $< 3$ ) which is consistent with the Zr/Nb of OIBs ( $< 10$ ). The Nb/Y vs. Zr/Y plot (Fig. 12b) also suggests an OIB origin for the samples, as most samples plot near the OIB field and near the “recycled component” average, which could also explain the Nd isotopic ratios which lack a specific mantle end-member signature. Interestingly, the ijolite sample (which also shows a distinct trend on MORB-normalized diagram; see Fig. 10) plots to the far left of the diagram, which indicates a garnet-bearing source. On a plot of Rb/Sr vs. Ba/Rb (Fig. 12A), samples indicate both phlogopite and amphibole as important source phases, with six of the silica-undersaturated samples plotting near primitive mantle values.

A lack of mantle xenoliths in the studied samples limits direct information about the mantle source. Moreover, Morris (1987) indicates the presence of granitoid, gneissic, and sedimentary xenoliths in some AAP members but not the presence of source xenoliths. High concentrations of incompatible trace elements in the samples (especially LILEs, see Figs. 10a, 10b) indicate that their mantle sources experienced some form of enrichment. In particular, Rb/Sr and Ba/Rb values indicate that phlogopite and amphibole were significant volatile-bearing phases for the samples (phlogopite for phonolite, syenite, and one lamprophyre sample, and

amphibole for one lamprophyre; see Fig. 12A). As discussed in Hawkesworth et al. (1984), these incompatible element ratios can be attributed to mantle enrichment process such as metasomatism. Therefore, the presence of phlogopite or amphibole in the mantle sources (Fig. 14 a-c) indicates that metasomatism by fluids or volatile-rich melts occurred prior to melting. La/Sm vs. Nb and Sr plots corroborates this, revealing that samples roughly plot along a line of carbonatite metasomatism (Fig. 17a, 17b). Melting of phlogopite-metasomatized mantle would explain the high K<sub>2</sub>O contents of the syenite samples (Downes et al., 2005). Additional indicators of carbonatite metasomatism in whole rock samples include the presence of apatite and a tendency towards wehrlite mineral assemblages (olivine, pyroxene, plagioclase, spinel, garnet, ilmenite, magnetite) which are seen in some BSE sample images (Fig. 14) (Rudnick et al., 1993).

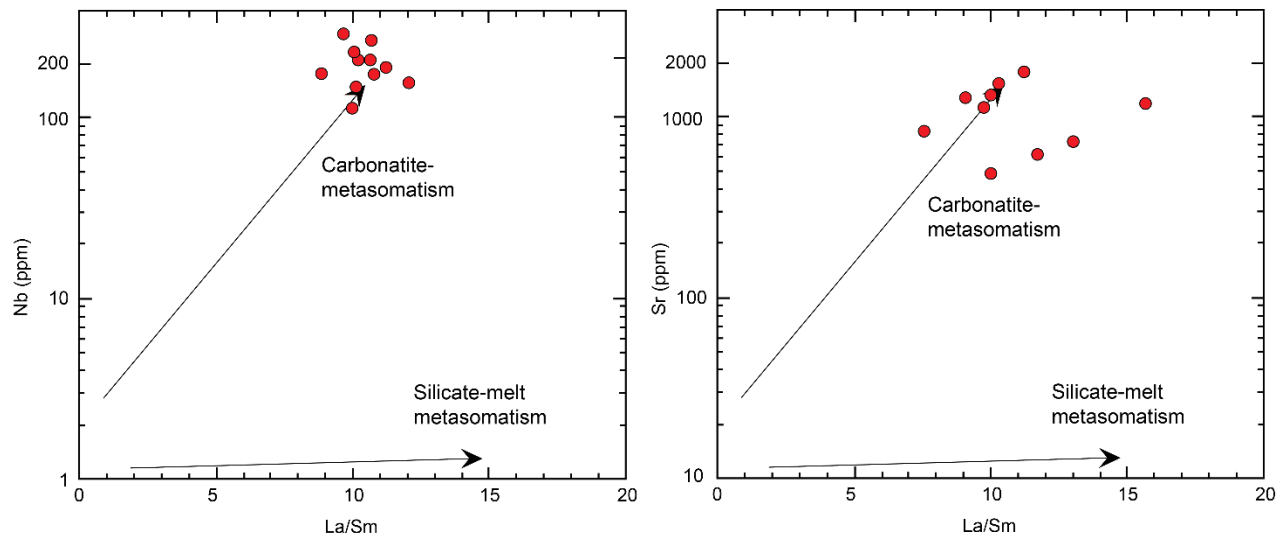


**Figure 17.** La/Sm vs. Sr and Nb plots which demonstrate the effects of carbonatite vs. silicate-melt metasomatism, after Downes et al. (2005).

### Paleostress Regimes

The orientations of mafic dike swarms can be used to investigate the paleostress fields that governed their emplacement in the crust. Dikes are generally emplaced parallel to the

regional horizontal maximum compressive stress direction ( $\sigma_1$ ) and perpendicular to the direction of extension ( $\sigma_3$ ) (Pollard, 1987; Baer and Beyth, 1990; Hoek and Seitz, 1995; Gudmundsson, 1995; Heermans et al., 1996; Hou et al., 2010). Extension in the crust can result from uplift of the lithosphere above hot asthenosphere (potentially caused by a mantle plume), or through forces caused by plate tectonics (Hoek and Seitz, 1995). The trends of AAP dikes and associated crustal structures are discussed in terms of their tectonic implications below.

Dike orientations discussed in this study vary but demonstrate prominent trends that are used to infer Cretaceous-age directions of extension. Group 1 dikes (> 100Ma) show a prominent NE-SW trend with a mean strike of  $058^\circ$  (Fig. 15a) and therefore reveal a NW-SE extensional stress regime at the time of their emplacement. These dikes follow the NE-SW-trending thrust faults of the Ouachita Mountains (mean strike:  $051^\circ$  - Fig. 15a); this suggests that dike emplacement in this area was controlled by local planes of weakness represented by potentially reactivated thrust planes during Cretaceous extension. Although group 2 dikes (< 100 Ma, >90 Ma) demonstrate a wider variety in trends (nearly every direction), a prominent E-W strike is apparent (Fig. 15b). A similar array of trends is observed for the thrust faults in the area - which also reveal a strong E-W strike - indicating that emplacement of Group 2 dikes was also controlled by local fabrics (Fig. 15b).

It has been previously suggested that MVG basement faults served as pathways that guided melt into the overlying crust in the Cretaceous Period (Matton and Jebrak, 2009; Eby and Vasconcelos, 2009). A comparison of dike trends and the strikes of MVG rift faults does yield some similarity. The nearest MVG faults in Arkansas strike at  $N34^\circ E$  and  $N75^\circ E$ , respectively, which are roughly similar to the NE-SW-trending Group 1 dikes, but less so with E-W-trending Group 2 dikes (Fig. 16b). The NW-SE-trending AOT, which serves as the termination of MVG

normal faults, does not demonstrate much similarity to dike trends (Fig. 16). Rough similarities between dikes and MVG faults could indicate influence of basement fabrics during their emplacement. However, due to stronger similarities between dikes and thrust faults, dike appear to have been more influenced by local and regional stress directions compared to MVG faults.

Due to the similarities between Cretaceous dikes and Pennsylvanian-Permian-age thrust plane orientations, there is a case for reactivation of Ouachita Mountain thrust faults during Cretaceous extension of the area. Extension must have reactivated thrust faults as normal faults, which allowed dikes to dilate along the strike of thrust faults. The reactivation of thrust faults caused by later crustal extension has been documented in several areas throughout the world (Bally et al., 1966; Platt, 1985; Guth, 1988; Cemen and Wright, 1990). Moreover, magma emplacement related to reactivated thrust faults has been discussed in detail in areas such as the Apennine Mountains, Italy (Musumeci et al., 2005; Dini et al., 2008), and the Mexican Fold and Thrust Belt (Ramirez-Pena et al., 2019). Dini et al. (2008) suggested that magmatic centers in the Apennine orogenic belt were focused by faults reactivated due to back-arc extension. Cemen and Wright (1990) determined that Cenozoic extension in the Death Valley area of the Basin and Range caused reactivation of Mesozoic thrust planes.

### **AAP Petrogenesis**

Competing hypotheses for mid-Cretaceous emplacement of the AAP and evolution of the adjacent ME each rely on differing emplacement mechanisms: (1) the existence of a mantle plume, presently situated in the Atlantic Ocean beneath the BR, or (2) a non-plume explanation which would involve tectonically-induced melting and emplacement of magma forming the AAP. The acceptance of either of these hypotheses requires proving or disproving the existence of a mantle plume that would explain: isotopic mantle values for AAP igneous bodies, OIB-like

trace element patterns, significant uplift of the proto-ME region (Cox and Van Arsdale, 1996; 2002) and the apparent age-progressive “hotspot” track between Kansas, Arkansas, and Mississippi.

There is little evidence that a mantle plume (herein referred to as the Bermuda mantle plume: Bmp) currently exists at its proposed location, 600-800 km east of the Eastern North American Margin. The location of the proposed plume – a topographic feature known as the Bermuda Rise (BR) – has been explained by multiple hotspot models (Davies, 1988; Sleep, 1990). Therefore, the Bmp’s existence has not been exhaustively denied, and more investigation is necessary. Courtillot et al. (2009) proposed a set of criteria necessary for a mantle plume to exist: (1) an age-progressive chain of volcanoes, (2) a flood basalt at this track’s origin, (3) a buoyancy flux, (4) high ratios of  $^4\text{He}/^3\text{He}$ , and (5) a low shear wave velocity in the underlying mantle. Courtillot et al. (2009) importantly distinguishes between “primary” (meeting all 5 criteria) plumes and “secondary” plumes, which do not meet all 5 criteria. An earlier paper by Courtillot et al. (2003) identified “tertiary” plumes, which are considered to be superficial in origin. The Bmp is barely eligible for criteria (1) and is thus termed a tertiary plume.

OIB magmas are commonly believed to represent plume-derived melts (Wilson, 1963; Zindler and Hart, 1986). Despite their noted heterogeneity, however, there are rough parameters for radiogenic isotope ratio values and trace element patterns for OIBs. As discussed in the previous section, trace element patterns exhibit smooth slopes similar to that of an average OIB and relatively less-enriched E-MORB, on MORB-normalized diagrams (Fig. 10b). However, trace element contents for the samples (excluding the ijolite) are significantly enriched over the OIB (Fig. 10b). Nd isotope ratios for the studied lamprophyres and other AAP members are indicative of more than one mantle source yet roughly plot within the range of OIB values (Fig.

13). This could be indicative of mantle mixing or a recycled component (likely an enriched component due to the trace element patterns).

It is worthy to note that Nd isotopic ratios obtained during this study are relatively depleted for the lamprophyre samples, which interestingly demonstrate significant enrichment in incompatible elements. This decoupling between isotopes and trace elements is also noted in Hawaiian lavas, and has been explained through multiple models which involve low degrees of partial melting of isotopically depleted mantle sources (which would result in chemically enriched melts) along with higher degrees of partial melting of isotopically enriched mantle sources (Winter, 2010, and references therein). This decoupling could be attained via shallow depleted mantle that is entrained in the margins of a mantle plume, and enriched deep mantle with recycled components which would produce tholeiites (see Figure 9). It is commonly understood that tholeiitic rocks can represent the hotter axis of a plume, while alkaline basalts should be more common towards the margins (Winter, 2010, and references therein). The close proximity of tholeiitic rocks and alkaline rocks could have been produced by upwelling of hot mantle material that was guided by previously existing lithospheric weaknesses.

Although potential OIB-like sources have been identified, one question remains: is it possible that the OIB signatures seen in the geochemical data were not derived from a mantle plume? It is noted in the literature that alkaline and transitional basalt in rift and non-rift settings are geochemically indistinguishable from true OIB (Fitton, 2007). Thus, OIB geochemical signatures for igneous rocks alone are not a diagnostic feature of mantle plumes, and the geochemical data must be viewed with caution when considering the plume hypothesis. It is necessary to consider other petrogenetic mechanisms that could produce similar geochemical signatures could be produced. In a specific example, McNutt (2006) suggested that oceanic

island volcanoes described in Hirano et al. (2001, 2006) are proof that mantle plumes are unnecessary to explain linear, age-progressive chains of igneous rocks, since the Pacific Plate's nearby subduction would likely block a rising mantle plume. Based on this line of reasoning, Fitton (2007) suggests that small degree melting of the upper mantle can produce OIB-like magma. Small degrees of melting are confirmed in the Nb/Y vs. Zr/Y plot, where samples plot by a recycled component (REC), and by the extreme enrichment seen in trace element diagrams (Fig. 12B). A relationship between recycled crustal components and a carbonatite metasomatizing agent has been suggested by Zindler and Hart (1986) and Weaver (1991). Metasomatism would also explain the decoupling between less-enriched isotopic ratios and enriched trace element patterns, given that low degrees of upper mantle melting would yield enriched trace element patterns (see Figs. 10a, 10b) yet less enriched isotopic values (see Fig. 13). The effects of metasomatism were also significant during petrogenesis, due to the enrichment in incompatible trace elements and La/Sm vs. Nb and Sr plots (Figs. 17a, 17b).

The presence of AAP rocks that are isotopically distinct from the lamprophyre samples in the study area doesn't discredit this explanation. Although isotopic and trace element data for this study indicate an asthenospheric upper mantle origin for the AAP members (V-intrusive, Benton dikes, Magnet Cove, Potash Sulfur Springs), other studies (Tilton et al., 1989; Duke et al., 2008) provide isotopic data that indicates an additional lithospheric source for the remaining members (Prairie Creek, Dare Mine Knob). Thus, in summary, a comprehensive petrogenesis of the AAP involves low degrees of partial melting of two distinct sources - lithospheric and asthenospheric mantle - with enriched components provided by metasomatic processes. A mechanism that provides the necessary heat and metasomatizing agent to generate the observed geochemical signatures is still required to fully explain the AAP's origins.

## **A Non-plume Mechanism for AAP Emplacement and ME Evolution**

Despite geochemical OIB signatures in the samples, the classification of the Bmp as a tertiary plume requires consideration of a non-plume mechanism. Proposed non-plume mechanisms for plume-like igneous provinces include extensional stresses which result in near-adiabatic rise, low-melting-point material transported upwards through convection, channelized fluids, leaky transform faults and fracture zones, and convective rise deflected by varying lithospheric thickness (Batiza, 1982; Anderson, 1998, 2005; Anderson and Schramm, 2005). In a particular example of non-plume mechanisms, Matton and Jebrak (2009) provide a comprehensive investigation of Cretaceous-age alkaline provinces across the world, known as the Peri-Atlantic Alkaline Pulse (PAAP). Due to a lack of convincing evidence for hotspots, Matton and Jebrak (2009) suggest that the PAAP (which includes the AAP) is controlled by lithospheric fracturing rather than mantle plume generation. In lieu of the mantle plume explanation, edge-driven convection (EDC) and continental insulation are potential mechanisms used to explain the spikes in magmatic activity at 125 Ma and 85 Ma (Matton and Jebrak, 2009) (Fig. 18). Their primary lines of reasoning involve the proximity between alkaline provinces and lithospheric weaknesses, and similar timing between magmatic spikes and major tectonic events. In this case, the AAP and associated ME lie near the AOT and MVG; both prominent lithospheric weaknesses. Moreover, rose diagrams for AAP dike orientations indicate a strong structural control on the dikes that are intruded into OFB thrust faults during Cretaceous extension (Fig. 15). These dikes lack a typical “radial” stress pattern that would have been induced by an underlying mantle plume (Smith, 1987) over a thermally uplifted area. An additional point of evidence involves the proximity of the AAP and the margin of the North American craton, where significant lithospheric thinning is evident (Schaeffer and Lebedev,

2014) (Fig. 18). It is possible that EDC cells were generated due to a difference in lithospheric thickness, demonstrated by the North American Craton which thins significantly towards the Atlantic Ocean.

Published emplacement ages for the dikes (106-89 Ma; see Eby and Vasconcelos, 2009) correlate generally with major tectonic events related to opening of the Atlantic Ocean, especially when considering the model of EDC by King and Anderson (1998), which suggests that convection reaches a peak velocity after about 80-100 Ma. Based on this timeline, EDC related to Central Atlantic opening would have been at its peak velocity between 120 and 80-90 Ma (Matton and Jebrak, 2009). This timing corresponds well with emplacement of Kansas (120 Ma) and Arkansas (106-89 Ma) igneous rocks, which both lie along the proposed Bmp track. Furthermore, EDC peak velocity would also explain uplift of the proto-ME as discussed in Cox and Van Arsdale (1996; 2002). The Jackson Dome intrusive (emplaced at 65 Ma – Dockery et al.) could indicate a lag in the upwelling portion of the EDC cell (modelled in Shahnas and Pysklywec, 2004) as North America continued to move westward.

In contrast to Atlantic rifting, EDC-related emplacement, and uplift of the AAP/ME could potentially be related to opening of the Gulf of Mexico (GOM). Krauss and Menke (2020) used seismic velocity measurements to suggest that the northern Gulf of Mexico may have experienced past small-scale convective upwelling near the North American continent's southeastern edge. Evidence for EDC is provided by a seismic anomaly known as the Northern Gulf Anomaly (NGA), which is delineated as a region of extremely low asthenospheric velocities (Krauss and Menke, 2020). The NGA is most intense at the Louisiana coast and in East Texas and forms a triangular wedge shape as far inland as 300 km (Krauss and Menke, 2020). In the context of the EDC model discussed in King and Anderson (1998), GOM

evolution and AAP emplacement correlate well in geologic time. EDC could have initiated as the GOM began opening ~180 Ma, which would result in EDC at its highest velocity around 100 or 80 Ma (which generally overlaps with AAP emplacement starting with lamproite magmatism at ~106 Ma; Eby and Vasconcelos, 2009). A model for ME evolution associated with GOM spreading would involve more N-S oriented EDC, as compared to Atlantic EDC, which provides E-W EDC cells (Matton and Jebrak, 2009).

A potential issue with this model involves the proposed age of this anomaly, and its relationship with emplacement ages of nearby alkaline provinces. The age of the anomaly itself has not been confirmed. Krauss and Menke (2020) suggest that, although the NGA could represent a fossil age associated with GOM opening, a younger age cannot be precluded. E-W oriented EDC makes sense with a rough age progression between Kansas, Arkansas, and Mississippi (suggested as evidence for a mantle plume; Eby and Vasconcelos, 2001), where continuous rifting in the Atlantic combined with a lag in magmatic upwelling creates an age-progressive track similar to a hotspot. The NW-SE orientation of the NGA (with a defined edge striking at 142°) could potentially explain the observed emplacement ages, as Kansas, Arkansas, and Mississippi provinces follow a general NW-SE trend. This model would involve emplacement of Kansas intrusives due to EDC, followed by Arkansas and then Mississippi volcanism as the GOM continues to open. A proposed model for AAP/ME evolution related to GOM opening is shown in Figure 20.

An alternative mode of EDC - facilitated by subduction of the Farallon Plate - is discussed in Duke et al. (2014). This study focuses primarily on mid-Cretaceous rocks (kimberlite, carbonatite, lamproite, etc.) between Montana and Arkansas, and suggests that magmatism between 110 and 94 Ma in Kansas and Arkansas was generated as kimberlite magma

migrated upward through tears in the eastern edge of the subducting Farallon Plate. The upwelling asthenospheric magma then melted subcontinental lithospheric mantle (SCLM) and crust which generated lamproite (Prairie Creek) magmas in Arkansas (Duke et al., 2014). Although generation of kimberlite magmas has been attributed to the release of slab-derived fluids (McCandless, 1999), the trace element signature diagnostic of subduction-related magmas (i.e. a negative Nb-Ta anomaly), is not observed in any of the samples analyzed during this study (Figs. 10a, 10b). Moreover, the data indicate that the metasomatic agent is likely carbonatite in composition (Figs. 17a, 17b) instead of fluid-related (which would be provided by a subducting slab).

This study argues that the generation of AAP magmas is not related to subduction of the Farallon Plate in geologic time and space, due to lack of a geochemical subduction signature, and geochronologic similarities between AAP emplacement and proposed timing of EDC related to regional tectonic events. EDC magmas are generally basaltic to alkali basaltic in composition, with upper asthenosphere and/or lower lithospheric mantle sources (e.g. Kjarsgaard, 2017; Kaislaniemi and van Hunen, 2014; Rudzitis et al., 2016). This is accommodated by AAP isotopic data, which demonstrate both lithospheric ( $\epsilon\text{Nd} = -19$  to  $-10$ ; Duke et al., 2008) and asthenospheric [ $\epsilon\text{Nd} = +2.7$  to  $+4.4$ , this study;  $\epsilon\text{Nd} = +1.9$  to  $+4.3$ ; Duke (2008; 2014)] sources. Based on the EDC model of Matton and Jebrak (2009), this study suggests that EDC related to rifting of the Atlantic Ocean brought upwelling asthenospheric material to the base of the lithosphere, which subsequently melted and produced lamproitic magmas of the Prairie Creek and Dare Mine Knob members of the AAP (as suggested in Duke et al., 2014). This line of reasoning is also applied to a model for EDC related to GOM opening (Figure 20) and based on the presence of a potentially EDC-related seismic anomaly in the northern Gulf (Krauss and

Menke, 2020). Following the generation of lamproites, deeper asthenospheric sources were tapped to produce lamprophyres, carbonatites, ijolites, etc. of the V-intrusive, Benton Dike Swarm, Magnet Cove, and Potash Sulfur Springs provinces.

## CONCLUSIONS

Trace element and Nd isotopic data indicate that mid-Cretaceous lamprophyres (V-intrusive and Benton Dike Swarm) of the AAP in Central Arkansas were generated by low degrees of partial melting of a depleted asthenospheric mantle source. The remaining sample lithologies – ijolite, jacupirangite, syenite, and phonolite – also demonstrate significant enrichment in incompatible trace elements and were likely derived from a similar asthenospheric source when compared with isotopic data from other studies (Duke et al., 2008; Duke et al., 2014). Both sources experienced metasomatism by a carbonatite agent (generated by a recycled

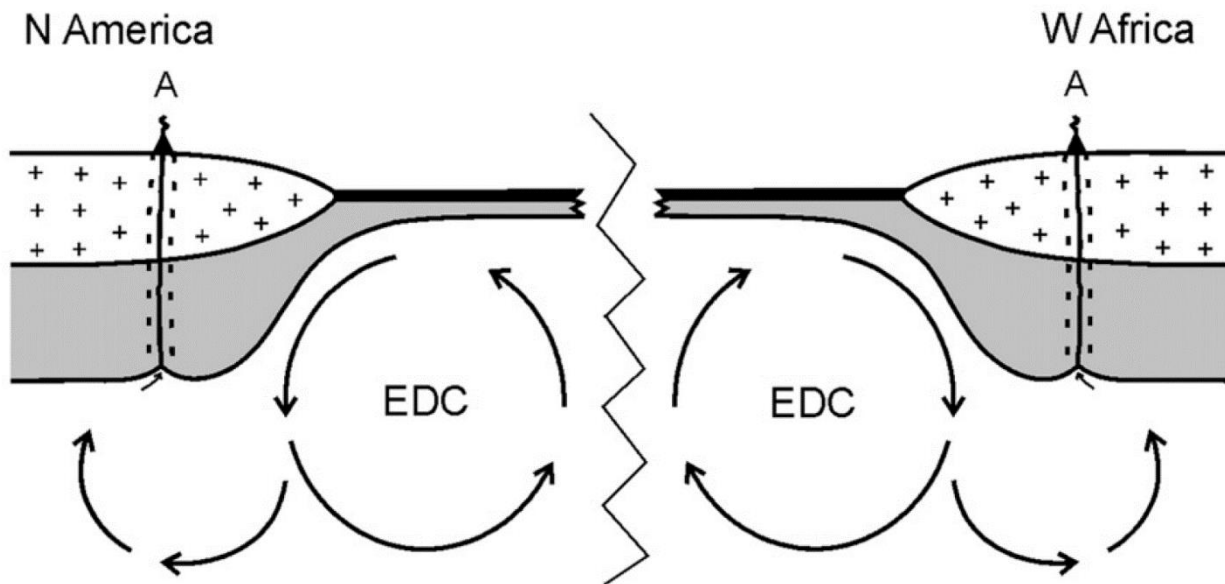
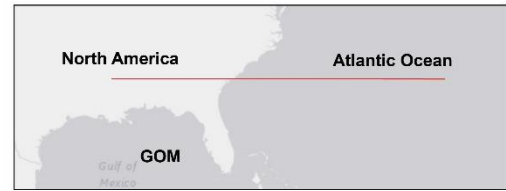
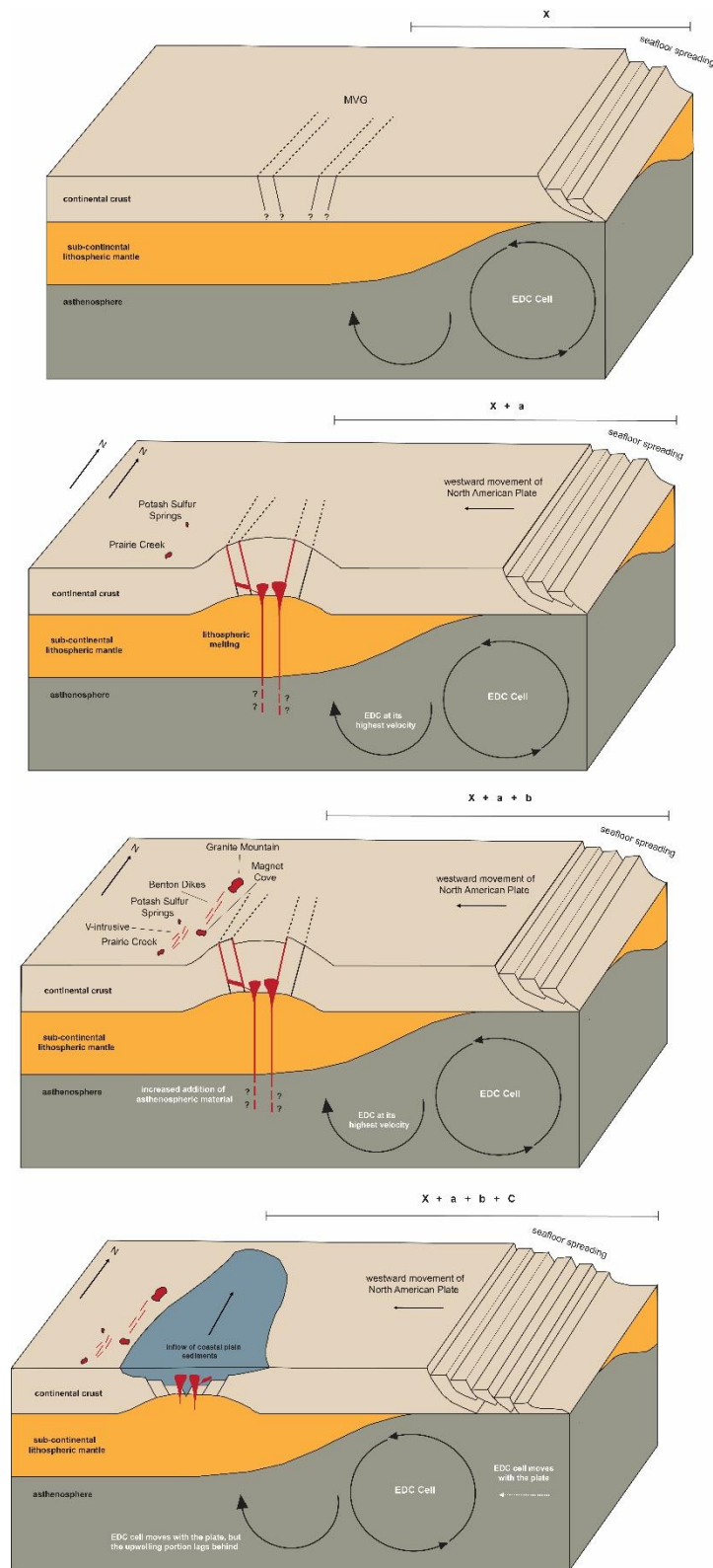


**Figure 18.** Schematic representation of EDC between two continental margins from Matton and Jebrak (2009). This diagram indicates EDC occurring as seafloor spreading occurs in the Central Atlantic, which causes upwelling of asthenospheric magmas. Reactivated structures in North America and West Africa are indicated by dashed lines surrounding solid lines. These lithospheric weaknesses guide the emplacement of EDC magmas.

component), which provided enrichment in incompatible elements, especially LILE. Although

trace element and isotopic data plot similarly with rough OIB values, this study argues for a non-plume mechanism of melting resulting in the generation and emplacement of the magmas. Based on similar timing between igneous ages and regional plate tectonic events (opening of the Atlantic Ocean, and the GOM), we propose that EDC – at its peak velocity 80-100 Ma after initiation of Atlantic rifting and GOM opening – uplifted the region of the proto-ME and guided melt along attenuated lithosphere at the edge of the North American Craton (Fig. 19).

Lithospheric weaknesses such as the MVG and AOT guided melt into the crust, where smaller dike emplacement was governed primarily by pre-existing thrust planes of the OFB. Upwelling asthenospheric material initially melted the base of the lithosphere resulting in lamproite magmas of the Prairie Creek and Dare Mine Knob members. Following lithospheric input, more asthenospheric material was incorporated in the melts, which resulted in generation and emplacement of lamprophyres, ijolite, jacupirangite, phonolite, syenite, etc. of the Magnet Cove, V-intrusive, Benton Dike Swarm, and Potash Sulfur Springs provinces. Therefore, tectono-magmatic evolution of the AAP and associated ME are best explained from a non-plume perspective, involving EDC initiated by plate tectonics (Figs. 19-20).



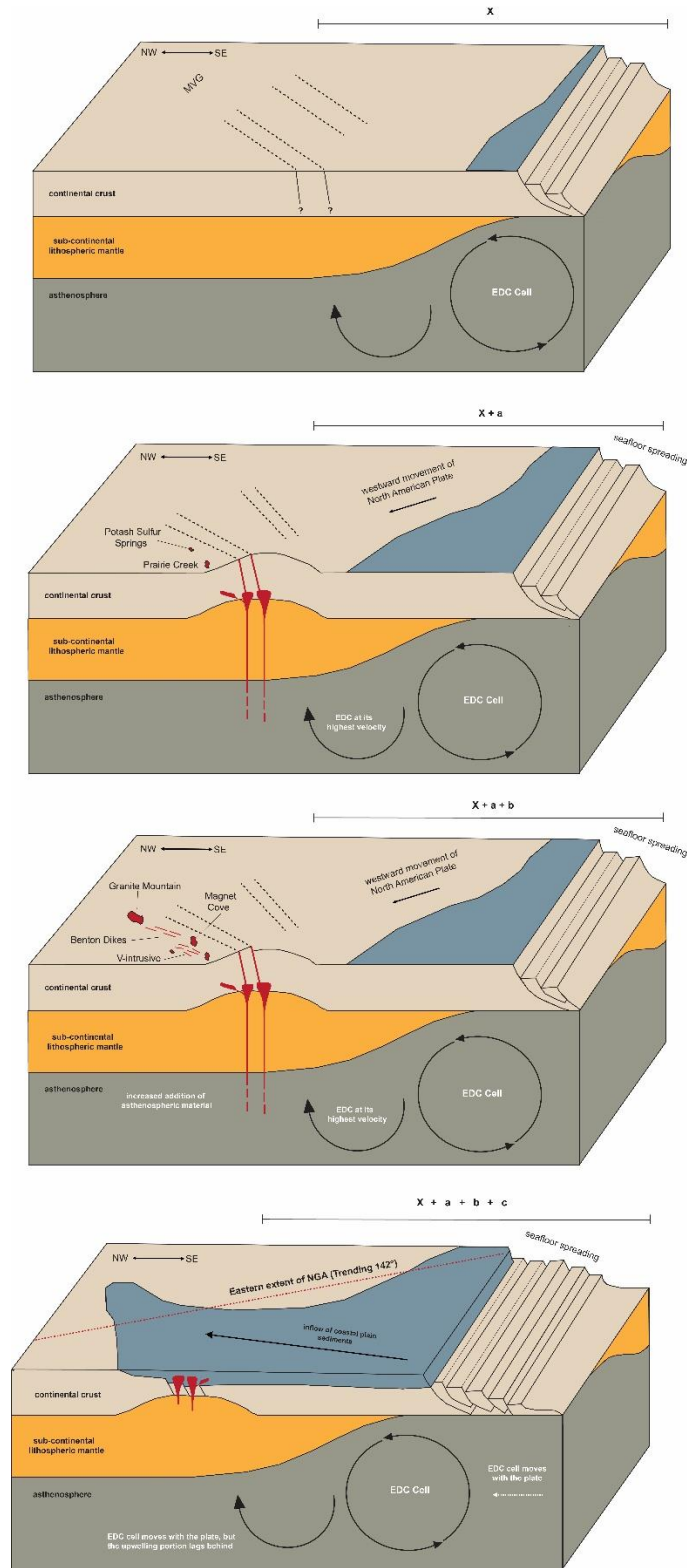
**Time 1 (~180-106 Ma):** spreading of the Atlantic Ocean begins and contrasting lithospheric thicknesses are sufficient to initiate EDC.

**Time 2 (~106-105 Ma):** EDC reaches its highest velocity, causing mantle upwelling and provides metasomatizing carbonatite melt before melting -  $\epsilon\text{Nd}$  SCLM (Dare Mine Knob and Prairie Creek).

**Time 3 (~104-89 Ma):** metasomatism, melting and upwelling of +  $\epsilon\text{Nd}$  magmas and emplacement of remaining AAP members. More asthenospheric material is incorporated in the melts at Time 3.

**Time 4 (~89 Ma - Present):** post-magma emplacement subsidence of the ME. Volcanic inactivity is attributed to a lag in the upwelling portion of the EDC cell as North America moves westward. Late Cretaceous sediments invade the ME.

**Figure 19.** Schematic diagrams indicating a time-progressive evolution for the ME and AAP. X represents the distance between MVG and the Atlantic rift, with extension indicated for time 2 (a), time 3 (b), and time 4 (c). Modified after Matton and Jebrak (2009) and Duke et al. (2014).



**Time 1 (~180-106 Ma):** opening of the Gulf of Mexico begins and contrasting lithospheric thicknesses are sufficient to initiate EDC.

**Time 2 (~106-105 Ma):** EDC reaches its highest velocity, causing mantle upwelling and provides metasomatizing carbonatite melt before melting -  $\epsilon\text{Nd}$  SCLM (Dare Mine Knob and Prairie Creek).

**Time 3 (~104-89 Ma):** metasomatism, melting and upwelling of  $+\epsilon\text{Nd}$  magmas and emplacement of remaining AAP members. More asthenospheric material is incorporated in the melts at Time 3.

**Time 4 (~89 Ma - Present):** post-magma emplacement subsidence of the ME. Volcanic inactivity is attributed to a lag in the upwelling portion of the EDC cell as North America moves westward. Late Cretaceous sediments invade the ME.

**Figure 20.** Schematic diagrams indicating a time-progressive evolution for the ME and AAP. X represents the distance between MVG and the GOM spreading center, with extension indicated for time 2 (a), time 3 (b), and time 4 (c). Modified after Matton and Jebrak (2009) and Duke et al. (2014). Eastern extent of the NGA is shown at Time 4 (Krauss and Menke, 2020).

## REFERENCES

- Anderson, D.L., 2005, Scoring hotspots: The plume and plate paradigms *in* Special Paper 388: Geological Society of America, p. 31-54.
- Anderson, D.L., 1998, The Edges of the Mantle: *Journal of Geodynamics*, v. 28, p. 255-271.
- Anderson, D.L., and Schramm, K.A., 2005, Global hotspot maps *in* Special Paper 388, Geological Society of America, p. 19-29.
- Autin, W.J., Burns, S.F., Miller, B.J., Saucier, R.T., and Snead, J.I., 1991, Quaternary geology of the Lower Mississippi Valley, *in* Morrison, R.B. ed., *Quaternary Nonglacial Geology*, Boulder, Colorado, Geological Society of America, p. 547–582, doi:10.1130/DNAG-GNA-K2.547.
- Baksi, A.K., 2001, Search for a deep-mantle component in mafic lavas using a Nb–Y–Zr plot: *Canadian Journal of Earth Sciences*, v. 38, p. 813-824.
- Baksi, A.K., 1997a, The Timing of Late Cretaceous Alkalic Igneous Activity in the Northern Gulf of Mexico Basin, Southeastern Usa: *The Journal of Geology*, v. 105, p. 629–644, doi:10.1086/515966.
- Baksi, A.K., 1997b, The Timing of Late Cretaceous Alkalic Igneous Activity in the Northern Gulf of Mexico Basin, Southeastern Usa: *The Journal of Geology*, v. 105, p. 629–644, doi:10.1086/515966.
- Bally, A.W., Gordy, P.L., and Stewart, G.A., 1966, Structure, seismic data, and orogenic evolution of southern Canadian Rocky Mountains: *Bulletin of Canadian Petroleum Geology*, v. 14, p. 337-381.
- Brookins, D.G., and Naeser, C.W., 1971, Age of Emplacement of Riley County, Kansas, Kimberlites and a Possible Minimum Age for the Dakota Sandstone: *Geological Society of America Bulletin*, v. 82, p. 1723, doi:10.1130/0016-7606(1971)82[1723:AOEORC]2.0.CO;2.
- Burke, K., and Dewey, J.F., 1973, Plume-Generated Triple Junctions: Key Indicators in Applying Plate Tectonics to Old Rocks: *The Journal of Geology*, v. 81, p. 406–433, doi:10.1086/627882

- Batiza, R. 1982, Abundances, distribution and sizes of volcanoes in the Pacific Ocean and implications for the origin of non-hotspot volcanoes: *Earth and Planetary Science Letters*, v. 60, p. 195-206.
- Cemen, I., and Wright, L.A. in the central and southern Funeral Mountains, Death Valley, California: , p. 12.
- Condie, K.C., 2003, Incompatible element ratios in oceanic basalts and komatiites: Tracking deep mantle sources and continental growth rates with time: *ELEMENT RATIOS IN OCEANIC BASALTS AND KOMATIITES: Geochemistry, Geophysics, Geosystems*, v. 4, p. 1–28, doi:10.1029/2002GC000333.
- Condie, K.C., 2001, *Mantle Plumes and their Record in Earth History*: Cambridge University Press, doi:10.1017/CBO9780511810589.
- Courtillot, V., Davaille, A., Besse, J., and Stock, J., 2003, Three distinct types of hotspots in the Earth's mantle: *Earth and Planetary Science Letters*, v. 205, p. 295–308, doi:10.1016/S0012-821X(02)01048-8.
- Cox, R.T., and Van Arsdale, R.B., 1997, Hotspot origin of the Mississippi embayment and its possible impact on contemporary seismicity: *Engineering Geology*, v. 46, p. 201–216, doi:10.1016/S0013-7952(97)00003-3.
- Cox, R.T., and Van Arsdale, R.B., 2002, The Mississippi Embayment, North America: a first order continental structure generated by the Cretaceous superplume mantle event: *Journal of Geodynamics*, v. 34, p. 163–176, doi:10.1016/S0264-3707(02)00019-4.
- Cullers, R.L., Dorais, M.J., Berendsen, P., and Chaudhuri, S., 1996, Mineralogy and petrology of cretaceous subsurface lamproite sills, southeastern Kansas, USA: *Lithos*, v. 38, p. 185–206, doi:10.1016/0024-4937(96)00010-2.
- Davies, G.F., 1988, Ocean bathymetry and mantle convection: 1. Large-scale flow and hotspots: *Journal of Geophysical Research: Solid Earth*, v. 93, p. 10467-10480, doi:10.1029/JB093iB09p10467.
- Dawood, Y.H., Abd El-Naby, H.H., and Sharafeldin, A.A., 2004, Influence of the alteration processes on the origin of uranium and europium anomalies in trachyte, central Eastern Desert, Egypt: *Journal of Geochemical Exploration*, v. 81, p. 15–27, doi:10.1016/S0375-6742(03)00210-3.
- Dini, A., Westerman, D.S., Innocenti, F., and Rocchi, S., 2008, Magma emplacement in a transfer zone: the Miocene mafic Orano dyke swarm of Elba Island, Tuscany, Italy: *Geological Society, London, Special Publications*, v. 302, p. 131–148, doi:10.1144/SP302.10.
- Dockery, D.T., Marble, J.C., and Henderson, J. 1997, The Jackson Volcano: *Mississippi Geology*, v. 18, p. 33-55.

- Duke, G.I., Carlson, R.W., Frost, C.D., Hearn, B.C., and Eby, G.N., 2014, Continent-scale linearity of kimberlite–carbonatite magmatism, mid-continent North America: *Earth and Planetary Science Letters*, v. 403, p. 1–14, doi:10.1016/j.epsl.2014.06.023.
- Duncan, R.A., 1984, Age progressive volcanism in the New England Seamounts and the opening of the central Atlantic Ocean: *Journal of Geophysical Research: Solid Earth*, v. 89, p. 9980–9990, doi:10.1029/JB089iB12p09980.
- Eby, G.N., and Vasconcelos, P., 2009, Geochronology of the Arkansas Alkaline Province, Southeastern United States: *The Journal of Geology*, v. 117, p. 615–626, doi:10.1086/605779.
- Ervin, C. P., and McGinnis, L. D., 1975, Reelfoot Rift: Reactivated Precursor to the Mississippi Embayment: *Geological Society of America*, v. 86, p. 1287-1295.
- Fitton, J.G., 2007, The OIB paradox, *in* Special Paper 430: Plates, Plumes and Planetary Processes, Geological Society of America, v. 430, p. 387–412, doi:10.1130/2007.2430(20).
- Fitton, J.G., Saunders, A.D., Norry, M.J., Hardarson, B.S., and Taylor, R.N., 1997, Thermal and chemical structure of the Iceland plume: *Earth and Planetary Science Letters*, v. 153, p. 197–208, doi:10.1016/S0012-821X(97)00170-2.
- Gogineni, S.V., Melton, C.E., and Giardini, A.A., 1978, Some petrological aspects of the Prairie Creek diamond-bearing kimberlite diatreme, Arkansas: *Contributions to Mineralogy and Petrology*, v. 66, p. 251–261, doi:10.1007/BF00373409.
- Hawkesworth, C.J., Rogers, N.W., van Calsteren, P.W.C., and Menzies, M.A., 1984, Mantle enrichment processes: *Nature*, v. 311, p. 331–335, doi:10.1038/311331a0.
- Hock, J.D., 1995, Continental mafic dyke swarms as tectonic indicators: an example from the Vestfold Hills, East Antarctica: *Precambrian Research*, p. 19.
- Hofmann, A.W., 1997, Mantle geochemistry: the message from oceanic volcanism: *Nature*, v. 385, p. 219–229, doi:10.1038/385219a0.
- Hou, G., Kusky, T.M., Wang, C., and Wang, Y., 2010, Mechanics of the giant radiating Mackenzie dyke swarm: A paleostress field modeling: *Journal of Geophysical Research*, v. 115, p. B02402, doi:10.1029/2007JB005475.
- Irvine, T.N., and Baragar, W.R.A., 1971, A Guide to the Chemical Classification of the Common Volcanic Rocks: *Canadian Journal of Earth Sciences*, v. 8, p. 523–548, doi:10.1139/e71-055.
- Kaislaniemi, L., and Van Hunen, J., 2014, Dynamics of lithospheric thinning and mantle melting by edge-driven convection: Application to Moroccan Atlas Mountains: *Geochemistry, Geophysics, and Geosystems*, v. 15., p. 3175-3189.
- King, S.D., and Anderson, D.L., 1998, Edge-driven convection: *Earth and Planetary Science Letters*, v. 160, p. 289–296, doi:10.1016/S0012-821X(98)00089-2.

- Kjarsgaard, B.A., Heaman, L.M., Sarkar, C., and Pearson, D.G., 2017, The North America mid-Cretaceous kimberlite corridor: Wet, edge-driven decompression melting of an OIB-type deep mantle source: MID-CRETACEOUS NORTH AMERICA KIMBERLITES: *Geochemistry, Geophysics, Geosystems*, v. 18, p. 2727–2747, doi:10.1002/2016GC006761.
- Krauss, Z., and Menke, W., 2020, The Northern Gulf Anomaly: P- and S-wave travel time delays illuminate a strong thermal feature beneath the Northern Gulf of Mexico: *Earth and Planetary Science Letter*, v. 534.
- Leitch, A.M., Davies, G.F., and Wells, M., 1998, A plume head melting under a rifting margin: *Earth and Planetary Science Letters*, v. 161, p. 161–177, doi:10.1016/S0012-821X(98)00147-2.
- Liu, L., Gao, S.S., Liu, K.H., and Mickus, K., 2017, Receiver function and gravity constraints on crustal structure and vertical movements of the Upper Mississippi Embayment and Ozark Uplift: Upper Mississippi Embayment Crust: *Journal of Geophysical Research: Solid Earth*, v. 122, p. 4572–4583, doi:10.1002/2017JB014201.
- Loper, D.E., 1998, Mantle plumes and their effect on the Earth's surface: a review and synthesis: *Dynamics of Atmospheres and Oceans*, v. 27, p. 35–54, doi:10.1016/S0377-0265(97)00026-2.
- Matton, G., and Jébrak, M., 2009a, The Cretaceous Peri-Atlantic Alkaline Pulse (PAAP): Deep mantle plume origin or shallow lithospheric break-up? *Tectonophysics*, v. 469, p. 1–12, doi:10.1016/j.tecto.2009.01.001.
- McCandless, T.E., and Gurney, J.J., 1999, Kimberlites: mantle expressions of deep-seated subduction: *Proceedings of the 7<sup>th</sup> international kimberlite conference*, v. 2, p. 545-549.
- Morgan, W.J., 1971, Convection Plumes in the Lower Mantle: *Nature*, v. 230, p. 42-43.
- Muller, R.D., 1993, Revised plate motions relative to the hotspots from combined Atlantic and Indian Ocean hotspot tracks: *Journal of Geology*, v. 21, p. 275-278.
- Musumeci, G., Mazzarini, F., Corti, G., Barsella, M., and Montanari, D., 2005, Magma emplacement in a thrust ramp anticline: The Gavorrano Granite (northern Apennines, Italy): *MAGMA EMPLACEMENT IN RAMP ANTICLINE*: *Tectonics*, v. 24, p. n/a-n/a, doi:10.1029/2005TC001801.
- Ramirez-Pena, C.F., Chavez-Cabello, G., Fitz-Diaz, E., Aranda-Gomez, J.J., and Sosa Valdes, R., 2019, Uplift and syn-orogenic magmatism in the Concepcion del Oro Block: A thick-skinned (Laramide style?) contractional structure in the Mexican Fold-Thrust Belt: *Journal of South American Earth Sciences*, v. 93, p. 242-252.
- Reiners, P.W., 2005, Zircon (U-Th)/He Thermochronometry: *Reviews in Mineralogy and Geochemistry*, v. 58, p. 151–179, doi:10.2138/rmg.2005.58.6.
- Rock, N.M.S., 1991, *Lamprophyres*: Springer Science & Business Media, 285 p.
- Rudzitis, S., Reid, M.R., and Blichert-Toft, J., 2016, On edge melting under the Colorado Plateau margin: *Geochemistry, Geophysics, Geosystems*, v. 17, p. 2835-2854.

- Schaeffer, A.J., Lebedev, S., 2014, Imaging the North American continent using waveform inversion of global and USArray data: *Earth and Planetary Science Letters*, v. 402, p. 26-41.
- Shahnas, M.H., 2004, Anomalous topography in the western Atlantic caused by edge-driven convection: *Geophysical Research Letters*, v. 31, p. L18611, doi:10.1029/2004GL020882.
- Sims, K.W.W., and DePaolo, D.J., 1997, Inferences about mantle magma sources from incompatible element concentration ratios in oceanic basalts: *Geochimica et Cosmochimica Acta*, v. 61, p. 765–784, doi:10.1016/S0016-7037(96)00372-9.
- Sleep, N.H., 1990, Hotspots and mantle plumes: Some phenomenology: *Journal of Geophysical Research*, v. 95, p. 6715, doi:10.1029/JB095iB05p06715.
- Stearns, R.G., 1957, Cretaceous, Paleocene, and lower Eocene, geologic history of the northern Mississippi embayment: *Geological Society of America*
- Stowell, H.H., and Tinkham, D.K., 2003, Integration of phase equilibria modelling and garnet Sm-Nd chronology for construction of P-T-t paths: examples from the Cordilleran Coast Plutonic Complex, USA: *Geological Society, London, Special Publications*, v. 220, p. 119–145, doi:10.1144/GSL.SP.2003.220.01.07.
- Sun, S.S. and McDonough, W.F., 1989, Chemical and isotopic systematics of oceanic basalts: implications for mantle composition and processes: *Geological Society, London, Special Publications*, v. 42, p. 313–345, doi:10.1144/GSL.SP.1989.042.01.19.
- Sundeen, D.A., and Cook, P.L. K-Ar dates from Upper Cretaceous volcanic rocks in the subsurface of west-central Mississippi: , p. 3.
- Thomas, W.A., 2006, Tectonic inheritance at a continental margin: *GSA Today*, v. 16, p. 4, doi:10.1130/1052-5173(2006)016[4:TIAACM]2.0.CO;2.
- Thomas, W.A., 1991, The Appalachian-Ouachita rifted margin of southeastern North America: *Geological Society of America Bulletin*, v. 103, p. 415-431.
- Thomas, W.A., 2011, The Iapetan rifted margin of southern Laurentia: *Geosphere*, v. 7, p. 97–120, doi:10.1130/GES00574.1.
- Tilton, G.R., Kwon, S.T., and Frost, D.M., 1987, Isotopic relationships in Arkansas Cretaceous alkalic complexes, *in Geological Society of America Special Papers*, Geological Society of America, v. 215, p. 241–248, doi:10.1130/SPE215-p241.
- Weaver, B.L, Trace element evidence for the origin of ocean-island basalts: *Journal of Geology*, v. 19, p. 123-126.
- White, R., and McKenzie, D., 1989, Magmatism at rift zones: The generation of volcanic continental margins and flood basalts: *Journal of Geophysical Research*, v. 94, p. 7685, doi:10.1029/JB094iB06p07685.

Wilson, M., 1997, Thermal evolution of the Central Atlantic passive margins: continental break-up above a Mesozoic super-plume: *Journal of the Geological Society*, v. 154, p. 491–495, doi:10.1144/gsjgs.154.3.0491.

Winter, J.D., 2010, *Principles of Igneous and Metamorphic Petrology*, Prentice Hall, 702 p.